Received Date : 07-Aug-2018
Revised Date : 02-Feb-2019

Accepted Date : 25-Feb-2019

Title: Metal binding to the dynamic cytoplasmic domain of the cation diffusion facilitator (CDF) protein MamM induces a 'locked-in' configuration

Authors: Shiran Barber-Zucker[1,2,3], Jenny Hall[4], Sivasubramanyan Venkata Mangapuram[5], Itamar Kass[2], Sofiya Kolusheva[3], Fraser MacMillan[4,*], Raz Zarivach[1,2,3,*] and Arnon Henn[5,*]

[1] Department of Life Sciences, Ben-Gurion University of the Negev, Beer Sheva 8410501, Israel

[2] The National Institute for Biotechnology in the Negev, Ben-Gurion University of the Negev, Beer Sheva 8410501, Israel

[3] Ilse Katz Institute for Nanoscale Science and Technology, Ben-Gurion University of the Negev, Beer Sheva 8410501, Israel

[4] School of Chemistry, University of East Anglia, Norwich Research Park, Norwich NR4 7TJ, United Kingdom

[5] Faculty of Biology, Technion- Israel Institute of Technology, Haifa, 3200003, Israel

* Corresponding authors:

Arnon Henn, Faculty of Biology, Technion- Israel Institute of Technology, Haifa, 3200003, Israel. Tel: +972 (4) 8294839; Fax: +972 (4) 8295424; Email: arnon.henn@technion.ac.il

Raz Zarivach, Department of Life Sciences, Ben-Gurion University of the Negev, Beer Sheva, 8410501, Israel. Tel: +972 (8) 6461999; Fax: +972 (8) 6472970; Email: zarivach@bgu.ac.il

Fraser MacMillan, School of Chemistry, University of East Anglia, Norwich Research Park, Norwich NR4 7TJ, United Kingdom. Tel: +44 (0) 1603-592766; Fax: +44 (0) 1603-592003; Email: Fraser.MacMillan@uea.ac.uk

Running title: Mechanism of metal binding to MamM CTD

Article type : Original Article

Abbreviations

CDF, cation diffusion facilitator; CTD, C-terminal domain; MTB, magnetotactic bacteria; PDB, Protein Data Bank; CD, circular dichroism; EPR, electron paramagnetic resonance; PELDOR, pulsed electron-electron double resonance; MD, molecular dynamics; ITC, isothermal titration calorimetry; WT, wildtype; CS, central site; PS, peripheral site; MMM, multiscale modelling of macromolecules; PCA, principal component analysis.

Database

Structural data are available in RCSB Protein Data Bank under the accession numbers: 6G64, 6G55, 6G5E and 6G6I (for CS, C267S, CS-C267S and W247A, respectively).

Keywords

Cation diffusion facilitator, Protein-metal interaction, Protein kinetics, PELDOR, Protein structure-function relationship.

Conflicts of Interest

The authors declare no conflicts of interest.

Abstract

Cation diffusion facilitator (CDF) proteins are a conserved family of transmembrane transporters that ensure cellular homeostasis of divalent transition metal cations. Metal cations bind to CDF protein's cytoplasmic C-terminal domain (CTD), leading to closure from its apo open V-shaped dimer to a tighter packed structure, followed by a conformational change of the transmembrane domain thus enabling transport of the metal cation. By implementing a comprehensive range of biochemical and biophysical methods, we studied the molecular mechanism of metal binding to the magnetotactic bacterial CDF protein MamM CTD. Our results reveal that the CTD is rather dynamic in its apo form, and that two dependent metal binding sites, a single central binding site and two symmetrical, peripheral sites, are available for metal binding. However, only cation binding to the peripheral sites leads to conformational changes that lock the protein in a compact state. Thus, this work reveals how metal binding is regulating the sequential uptakes of metal cations by MamM, and extends our understanding of the complex regulation mechanism of CDF proteins.

Introduction

Protein-metal cation interactions are key players in the function of many biological process, whether they serve as structural anchors (as in zinc fingers [1]), participate directly in enzymatic reactions (as in the calcium/manganese cluster in photosystem II [2] or copper in tyrosinases' active site [3]) or stabilize enzymes' active sites (as in magnesium in metallonucleases' active sites [4]). Since metal cations are rather small ligands they can easily diffuse into empty but charged binding sites, thus metal-ligand binding processes usually occur quite quickly [5]. These cations must bind selectively in their specific binding sites to ensure the correct conformational changes and function [6]. Understanding the exact mechanism of this type of binding, especially in terms of how these interactions occur and lead to conformational changes on short time scales, is of huge value for the study of the overall mechanism of a specific protein. However, the molecular mechanism of protein-metal binding is often not well characterized, and such knowledge is lacking in many protein families.

The cation diffusion facilitator (CDF) family is an example of a protein class where such protein metal binding is not well understood. CDFs are a divalent transition metal cation transporter family that maintain such cation homeostasis, and are conserved throughout all domains of life [7]. CDF proteins export a range of divalent metal cations, such as Zn^{2+}, Mn^{2+}, Fe^{2+}, Cd^{2+} and Co^{2+} out of the cytoplasm, typically by exploiting the proton motive force while undergoing conformational change [8–10]. CDF proteins form hetero- or homodimers and contain two major domains: the transmembrane domain and the cytoplasmic C-terminal domain (CTD). The transmembrane domain is found in all known CDF proteins and includes six helices per monomer as well as a well-characterized metal binding site through which the metal cations are transported [9–11]. The CTD domain is abundant in CDF proteins, adopting a metallochaparone-like fold and undertaking metal-binding-related conformational changes [12,13]. The CTD has been better characterized both structurally and biochemically than the transmembrane domain, and it has been proposed to act as a regulatory domain. The CTD contains metal binding sites which are found on the protein surface, thus exposed to cytoplasmatic metal ions. With quite low affinity to metals, it has been speculated that in high cytoplasmic metal concentrations, the metal cations are bound to these CTD binding sites. This causes a conformational change where the two monomers, that were found in an apo V-shaped conformation, approach each other to form a tighter V-shaped conformation. This, in turn, induces a conformational change of the transmembrane domain allowing the efficient, fast transport of cations through this domain (which has greater affinity) [8,13]. Namely, only at high levels of metals (concentrations that approach cytotoxicity) will they be bound to the CTD to activate the actual transport. In contrast to the transmembrane binding site, the metal binding sites in the CTD are not fully conserved in terms of properties, location and number (although in most proteins more than one binding site has been proposed) [14]. The exact binding mechanism and its energetics, the kinetic pathway by which metal binding induces these proposed structural changes, and how the ions bind and interact with the CTD, remain poorly understood. A number of specific questions are yet to be addressed, including how the metal binding sites are populated during activation, and if there is an ordered binding sequence. Furthermore, whether allostery and cooperativity exist and play a functional role in CTD activation, and finally if all metal binding sites are required to fully induce the conformational change and activation of the CTD.

To address these questions, the metal binding mechanism in MamM CTD, a CDF protein from magnetotactic bacteria (MTB), has been investigated. MTB are a group of Gram-negative bacteria that biosynthesize iron-based magnetic particles in designated organelles named magnetosomes. These magnetosomes are arranged in a chain-like fashion, thus enabling them to align themselves to the geomagnetic field in order to reach their preferred habitat, usually the oxic-anoxic zones in aquatic environments [15,16]. MamM transports iron from the bacterium cytoplasm into such magnetosomes, which enables synthesis of iron-based magnetic particles inside the vesicles. In the absence of MamM or in case of mutations that cause its dysfunction, these particles are either not formed or formed

defectively [13,17–19]. Since such differences in magnetic particle formation in MTB are easy to study, MamM serves as an effective model to study CDF proteins. The MamM CTD structure has been solved in its apo form, and a comprehensive biophysical study has revealed that it undergoes conformational change when it binds Fe^{2+} and Zn^{2+} in three proposed binding sites: two symmetrical peripheral binding sites and one central binding site. Mutations in these postulated binding site residues lead to a decreased function both *in vivo* and *in vitro* [13]. Here a combination of different biophysical methods is used to study MamM CTD dynamics and kinetics, in order to decipher the protein-metal binding mechanism. Overall, the unique combination of X-ray crystallography, circular dichroism (CD) spectroscopy, pulsed electron paramagnetic resonance (EPR and PELDOR) spectroscopy, molecular dynamics (MD), isothermal titration calorimetry (ITC), fluorescence spectrometry and stopped flow results reveal a dependence between the central and peripheral binding sites, and that rapid binding occurs at the central binding site while only binding to the peripheral sites induces significant conformational change. These results reveal the complexity of metal binding to MamM specifically and to CDF proteins' cytoplasmic domain in general, and constitute a significant step towards the understanding of the diverse regulation mechanisms in CDF proteins and their contribution to CDF protein function.

Results

Previously it was shown that metal binding to MamM CTD *in vitro* occurs only at basic pH due to the involvement of histidine residues in the coordination of the metal ions [13]. Fe^{2+} tends to precipitate at basic pH, however its effective concentration is highly important for stoichiometry determination and interpretation of the kinetic mechanism of ligand binding. Hence, for this reason and also to enable a comparison with previous studies utilizing Zn^{2+} as a model for metal binding [13], we performed a structural, thermodynamic and kinetic investigation of Zn^{2+} to study the metal binding mechanism in MamM CTD.

Structural studies of MamM CTDs indicate binding-dependent conformational change

MamM CTD is arranged as a stable dimer forming two putative symmetrical peripheral sites (histidine 264 and glutamate 289 of monomer one and two, respectively) and one central binding site formed with a quartet of residues (aspartate 249 and histidine 285 from each monomer) (Figure 1A) [13]. To understand the MamM CTD-Zn^{2+} binding mechanism, constructs termed WT (wildtype MamM C-terminal domain residues 215-318), PS (peripheral site; WT with D249A and H285A mutations which abolishes the central binding site, construct contains only the peripheral sites) and

CS (central site; WT with H264A and E289A mutations which abolishes the peripheral binding sites, construct contains only the central site) were used.

The crystal structure of the apo WT protein, which has been solved previously, displays the characteristic fold of CDF proteins (PDB ID: **3W5X**, **3W5Y**) [13]. The crystal structures of both the apo PS construct (PDB ID: **3W8P**, **3W66**) [13] as well as the apo CS construct (PDB ID: **6G64**, Tables 1-3, Figure 1B) which was solved for this study reveal no differences as compared to the WT structure (see Table 4 for RMSD data between the different structures), suggesting that the apo forms do not differ in their three dimensional crystal structures. Since, it has not yet proven possible to crystallize the different MamM CTD constructs in the presence of Zn^{2+}, other structural methods have been applied to better understand the conformational changes occurring due to metal binding. Circular dichroism (CD) spectra of all apo protein constructs (WT, PS and CS) confirmed that the secondary structures of all three proteins are also conserved in solution (Figure 2). The CD spectral trends after addition of Zn^{2+} (protein:Zn^{2+} at 1:15 ratio) are consistent with the apo forms, suggesting that the conformational changes occurring due to metal binding do not involve substantial changes in their secondary structures, but most likely at the dimerization interface, similar to the CDF protein CzrB [12].

To further understand the MamM CTD metal-dependent conformational changes, site-directed spin labelling was applied in combination with pulsed electron-electron double resonance (PELDOR) spectroscopy [20,21], which affords the detection of both distances and distance distributions between labelled sites within the dimer. During site-directed spin labelling, the paramagnetic (1-oxyl-2,2,5,5-tetramethylpyrrolidin-3-yl)methylthiosulfonate spin label (MTSSL) reacts specifically with cysteine residues of the protein. MamM CTD contains two intrinsic cysteine residues, C267 and C275, the second of which is found on the periphery of the protein in a solvent-exposed region. Both *in silico* modelling and spin labelling efficiencies indicate that C267 does not label well, hence PELDOR experiments were performed using the C267S variant protein which provides only distances between the two labelled C275 sites on the protein (Figure 1C). *In silico* prediction of inter-spin label distances was carried out using Multiscale Modelling of Macromolecules (MMM) [22], a Matlab©-based open-source modelling toolbox.

This C267S mutation was introduced by site-directed mutagenesis to all three MamM CTD constructs: C267S (WT with C267S mutation), PS-C267S (PS with C267S mutation) and CS-C267S (CS with C267S mutation). Crystallization trials were performed on these constructs to confirm that the C267S mutation also does not alter the protein structure. Only the C267S and CS-C267S constructs formed crystals allowing a structure to be determined (PDB IDs: **6G55** and **6G5E**, respectively, see Tables 1-3 and Figure 1B). In both cases the structure revealed no difference to the wild type structure. All variant proteins labelled efficiently, indicating good accessibility of the C275 site. Further, by using the structure of the apo C267S form, the MMM study predicted an inter spin distance of 4.0 nm between the labelled cysteines at this position (C275, Figure 1C).

In Figure 3 PELDOR experiments of all three apo forms (as well as Zn^{2+}-bound) are presented. The upper panels of Figure 3 present the background-subtracted time-domain traces for both apo and metal-bound protein, while the lower panels represent the distance distribution probability of the metal bound-state after data analysis using DeerAnalysis 2016 [23]. Both the apo forms of C267S and CS-C267S revealed no defined distance between the two labelled cysteines, suggesting that these proteins do not adopt a single stable conformation in this state, but are rather dynamic (Figure 3A-B). In the PS-C267S apo protein, however, a strong initial decay of the PELDOR signal in the time domain was observed which is quite different from the C267S and CS-C267S time domain spectra (Figure 3C). Such initial steep decays can be indicative of very short distances, typically < 2 nm between the labels. In the apo WT protein, the negatively charged aspartate and bulky histidine residues that form the putative central site protrude towards one another in the space between monomers, resulting in clashes and/or charge repulsion. This could increase the distance between monomers. Removal of these residues from the dimer interface could in principle allow for more stable and tighter packing as compared to the apo WT protein, however the direct closure of the V-shape dimer would not be in agreement with a short inter spin distance inferred from the PELDOR time-domain results. It was previously suggested that the two monomers could also swivel along a perpendicular axis [13] rather than simply moving laterally towards one another. Hence removal of these charged, bulky residues in PS-C267S could allow for a larger degree of swiveling movement and thus explain the proposed short inter spin distance in PS-C267S.

Addition of zinc chloride (x 5 excess) to each MamM CTD form (C267S-Zn^{2+}, PS-C267S-Zn^{2+} and CS-C267S-Zn^{2+}) results in large changes in the PELDOR time-domain traces (Figure 3 upper panels). For C267S-Zn^{2+} a narrow distance distribution was determined with a mean distance of 3.3 nm (Figure 3A, lower panel), indicative of a predominantly closed conformation upon metal binding which is rigid compared to the apo form and slightly shorter than the MMM prediction. A systematic Zn^{2+} titration (from 1:1 to 1:10 protein:metal ratios) revealed that the observed modulation depth increases with the successive addition of Zn^{2+} up until a ratio of 1:3-1:4 where it reaches a saturation point, which can be indicative of 3-4 Zn^{2+} ions bound per dimer (Figure 4 left panels and Table 5). Beyond this ratio no further increase in modulation depth is observed and indeed there is only a slight decrease which is due to the high metal ion and protein concentrations, which is known to cause aggregation in solution. An increase in modulation depth was also observed for CS-C267S-Zn^{2+} compared to its apo state, however the distance distribution obtained was extremely broad, indicating that a single stable conformation was not adopted in the presence of the Zn^{2+} (Figure 3B). This suggests that whilst the addition of metal has some effect on the structure and dynamics of the protein, an entirely closed and rigid Zn^{2+}-bound state is unlikely to be present. Hence, mutation of the peripheral binding sites does affect metal binding and does not allow meaningful conformational changes to be observed. For PS-C267S-Zn^{2+}, again a predominant, but distinct narrow distance distribution is obtained, with a mean distance of 2.7 nm (Figure 3C). This result would suggest that

the addition of Zn^{2+} causes PS-C267S to adopt a slightly different rigid conformation, where the spin labels are now further apart as compared to the apo state. Such a 2.7 nm distance would fit with a tight V-shape packing that is not possible in the WT protein due to the presence of the histidine and aspartate residues in the metal binding site, which are proposed to increase the gap between the monomers as compared to this alanine mutant. Repeating the Zn^{2+} titration experiment with PS-C267S MamM CTD with Zn^{2+} (from 1:1 to 1:5 protein:metal ratios) reveals an increase in modulation depth with successive addition of Zn^{2+} up until a ratio of 1:2, at which point saturation is already reached and no further increase is observed (Figure 4 right panels and Table 5). This clearly indicates that less Zn^{2+} ions are bound per dimer of PS and indeed fits well with the proposal that only two Zn^{2+} ions are bound, one in each peripheral site. In summary, it is proposed that Zn^{2+} addition to PS results in its binding to the peripheral sites only, which restricts the swiveling movement and stabilizes the protein in a "native-like" closed conformation, but with tighter packing due to removal of the bulky residues at the central site.

Overall, the PELDOR results obtained, both when comparing apo and Zn^{2+}-bound states of each variant forms as well as between the Zn^{2+}-bound forms of the different MamM CTDs, suggest that the protein adopts a closer packing in solution upon addition of metal ions, and that the residues in both peripheral and central sites have an influence on, and are important for metal binding and conformational change.

Apo-MamM CTDs demonstrate different dimerization dynamics

In order to study the effect of mutations on apo-MamM dynamics, and to assess whether the proposed swiveling movement is possible, molecular dynamics (MD) simulations were also used. As CS was shown to behave similarly to WT in their apo forms, MD was only applied to WT and PS. Later, the MD trajectories were studied using principal component analysis (PCA). PCA, also known as essential dynamics, is an analysis method that reduce the dimensionality of a complex system while retaining the most important features of the distribution of conformations [24–26].

Initially, the stability of each simulated protein was validated, and the root mean square deviation (RMSD) values of the backbone were calculated. As MamM CTD is a homodimer, the RMSDs for each monomer and of the dimer were calculated separately. Calculated values of backbone RMSD for the production stage (after the initial 20 nsec) of each simulation are 0.13 ± 0.02 nm (monomer 1, WT), 0.11 ± 0.01 nm (monomer 2, WT), 0.31 ± 0.10 nm (dimer, WT), 0.11 ± 0.01 nm (monomer 1, PS), 0.13 ± 0.02 nm (monomer 2, PS) and 0.31 ± 0.13 nm (dimer, PS). The outcome indicates that following an initial reengagement, the 3D structure of all monomers is highly stable. On the other hand, while both WT and PS maintain their dimers, their averaged RMSDs are higher. In addition, their RMSDs show a higher rate of fluctuation (data not shown). This RMSD profile is likely to be due to the movement of one monomer towards the other.

To further study the dynamics of MamM dimers, the first two modes of motions (modes 7 and 8) calculated using PCA were used. Modes 7 and 8 are the largest collective motions of groups of atoms following the removal of translation (modes 1 to 3) and rotation (mode 4 to 6) movements of the WT and PS complexes. The translation and rotations are removed as they are not contributing to the molecule flexibility. First, the calculated fluctuations of modes 7 and 8 were compared with the those calculated from the MD trajectories. The fluctuation profiles were found to be very similar (Pearson correlation coefficient are R=0.97 and 0.96 for WT and PS, respectively), indicating that modes 7 (the native-like open-close movement) and 8 (the swiveling movement) account for most of the overall protein motion. Furthermore, this confirms that low-frequency motions govern MamM-complex's overall dynamics. A comparison of WT and PS revealed that PS is more flexible than WT (Figure 5). Whereas most fluctuations in the WT are located at the top of the beta-sheet, in PS a larger portion of the protein fluctuates. Moreover, the magnitude of fluctuations in PS is larger compared to the WT's. In addition, fluctuations at mode 8 of PS reveals a large amplitude of swiveling movements, unlike WT (Figure 5, bottom panel). Taken together, the simulations suggest that the lack of the binding residues in the central site effects the apo-MamM dynamics as was also proposed by the EPR results, with the apo-PS undergoing a more pronounced dynamic swiveling movement.

Stoichiometry of Zn^{2+} binding to MamM CTD constructs

The occupancy of the three MamM CTD binding sites during its activation in solution have not been determined previously. PELDOR results would suggest that 3 or 4 ions are bound to the WT construct while only 2 ions bind to the PS construct. In order to formulate a kinetic model for metal binding during activation of MamM CTD, the binding stoichiometry of divalent ions must be precisely determined for all protein constructs. For that, Zn^{2+} and the three MamM CTD constructs WT, PS and CS were utilized. Equilibrium ligand binding was performed by isothermal titration calorimetry (ITC) to determine MamM CTD-Zn^{2+} binding thermodynamic parameters and stoichiometry, i.e., how many metal ions are bound per MamM CTD homodimer. In Table 5 the summary of the ITC experiments with WT and the PS mutant is presented. The CS revealed no heat change on Zn^{2+} concentration-dependent binding (Figure 6). The PELDOR experiments and fluorescence measurements (see below) did however indicate Zn^{2+} concentration-dependent binding. It can be speculated that Zn^{2+} binding to CS does not generate a large enough heat capacity change in the system to be detected. When considering that Zn^{2+} binding to the central binding site leads to minor conformational changes, as is evident from results obtained by the other methods employed, it is more probable that the entropy and enthalpy changes are balanced such that overall nearly no change in the Gibbs free energy of the system is observed. Both WT and PS show similar parameters (Table 5), but PS shows a slightly preferred binding to Zn^{2+} in terms of thermodynamics parameters (~ 57% lower $K_{D,}$ as well as slightly

lower ΔG, which is characterized by both smaller ΔH and larger ΔS). However, WT shows a greater N value (2.80 ± 0.24) as compared to PS (2.41 ± 0.24). This would mean that while WT can bind ~ 3 Zn^{2+} ions per dimer, in clear agreement with the PELDOR titration data, PS can only bind ~ 2-2.5 ions but with slightly higher affinity, again corroborated by the PELDOR data. These ITC results suggest that each peripheral site can bind one ion, and the central site is occupied by a single ion that has almost no impact on the heat of the system. In the case of the PS construct, the mutated central site that lacks the histidine and aspartate residues cannot bind the Zn^{2+} ion effectively, but the binding to this PS construct is thermodynamically preferred, most likely due to a more stable conformational change caused by Zn^{2+} binding to the peripheral sites, as compared to the WT protein.

Interpretation of the fluorescence signal arising from metal binding to MamM CTD

Upon analysis of the MamM CTD sequence one tryptophan (W247) residue per monomer was identified, juxtaposed to the central binding site (Figure 1A), and one tyrosine residue, Y241, that is remote from both the central and peripheral binding sites, but which may still contribute to any intrinsic fluorescence change upon binding of metals after excitation at λ_{ex} 280 nm. Indeed, metal binding to MamM CTD has been shown to induce a change in the intrinsic fluorescence signal upon excitation at λ_{ex} 280 nm [13]. To detect whether similar differences in the fluorescence signal occur due to Zn^{2+} binding in the different MamM CTD constructs, fluorescence measurements were conducted upon Zn^{2+} binding to MamM CTD as a function of Zn^{2+} concentration (Zn^{2+}:MamM CTD ratios were varied from 0:1 to 100:0) (Figure 7A-C). In order to be assured that the fluorescence signal observed is only contributed by the W247 residue and not by the Y241 residue, a more specific excitation wavelength of λ_{ex} 297 nm was used which is towards the tryptophan. Indeed, a point mutation to remove this particular tryptophan residue, W247A (WT with W247A mutation), abolishes completely the fluorescence signal (Figure 7D). The crystal structure of this mutant (Figure 1D), which also confirms the substitution, reveals the same monomeric fold as that of the WT, and a very similar dimerization interface with only a minor shift of the monomers towards one another, probably due to the crystal packing. The tryptophan fluorescence emission spectra of the MamM CTD proteins reveal a Zn^{2+} concentration-dependent blue shift of the spectrum for all the different MamM CTD constructs, as well as an increase in fluorescence intensity. These results suggest a shift of W247 towards a more hydrophobic environment in the presence of Zn^{2+}, hinting at a Zn^{2+}-dependent conformational change. When comparing the MamM CTD WT data with those of PS (Figure 7A, B, E, F), WT demonstrates a greater blue shift and an increase in fluorescence intensity in the presence of Zn^{2+}. This is most likely due to: (1) The alanine substitution at position 249 in PS which is juxtaposed to the W247 residue, which will influence the initial tryptophan environment hydrophobicity and leads to a lower initial λ_{max}, and (2) a closer, or different, apo V-shaped conformer

in solution, which is possible due to the lack of D249-D249 repulsion and the removal of the bulky H285 residues from the center of the V-shape dimer, as is also proposed from both the PELDOR and MD data. In contrast, upon addition of Zn^{2+} to the CS construct, there is a large increase in intensity as compared to the other MamM CTD constructs while only a minor blue shift is observed. This would suggest that the CS construct is somehow affected differently by the presence of Zn^{2+} which is reinforced by the lack of clear detectable binding as determined by both the ITC and PELDOR spectroscopy. The Zn^{2+} concentration-dependent maximum wavelength plots were fitted to a hyperbolic equation with K_D values determined using the point of half saturation for protein-Zn^{2+} binding (WT and PS are 18.66 ± 3.54 μM and 82.72 ± 9.23 μM, respectively). These values differ from values calculated from the ITC, but with similar order of magnitude. These differences are most likely due to the fluorescence curves reflecting only binding that is affected by the fluorescence signal and therefore should only provide a first estimate of metal affinities to MamM CTD. Importantly, the ITC values should be considered as the hard parameters for the model. Nonetheless, both methods give K_D values of the same order of magnitude although the concentrations used in the fluorescence measurements were 10 times lower than that used in the ITC, suggesting that indeed the affinity is in the micromolar range, as can be expected from protein-surface bound metals in general, and from the CDFs' CTD in particular [13,27].

Kinetics of Zn^{2+} binding to MamM CTD constructs

The kinetics of Zn^{2+} binding to MamM CTD has been measured to investigate the dynamics of metal binding and to identify any biochemical intermediates during the time course of its binding reaction. Upon Zn^{2+} binding, an increase in the intrinsic tryptophan fluorescence of both WT and PS can be nicely observed (Figure 8A, B). However, for CS no time-dependent changes in tryptophan fluorescence are detected (Figure 8C). Nevertheless, careful inspection of CS time traces suggests that a rapid binding event, within the dead time of the stopped flow experiment (1.5 msec), might be occurring, due to the higher fluorescence already observed at time zero as a function of the increasing Zn^{2+} concentration. In addition, the fluorescence changes upon Zn^{2+} binding to the CS construct are nicely shown in Figure 7C, E, F.

The time courses of the fluorescence increase upon rapid mixing of Zn^{2+} with WT, follows a single exponential up to 500 msec. Beyond this time regime the fluorescence intensity decreases, most likely due to relatively high photobleaching of the W247 residue in each monomer. The ITC stoichiometric model fitting predicts three Zn^{2+} ions binding per WT dimer (Table 5). Structurally, this can account for the two identical peripheral sites and the one central site which is formed at the interface of the two monomers. Multiple binding sites which are not identical in terms of their chemical composition are less likely to yield an identical spectroscopic signature. Therefore, it was not expected that rapid binding kinetics exhibits only a single kinetic phase as shown by the mono-exponential fluorescence

intensity. The observed single phase may be due to binding occurring during the stopped flow dead time (~1.5 msec) to either sites, to a fluorescence silent binding site or to a combination of both. Based on the WT and the mutants' PELDOR, fluorescence and ITC data, we favour that the measured fluorescence increase in the transient time course reflects the binding of Zn^{2+} to the peripheral sites according to the general Scheme 1. The initial binding of Zn^{2+} to the central site is rapid, occurring within the dead time of the stopped flow with a binding rate > 1,000 sec^{-1} (shown in squared parenthesis: CTD^O and CTD^C are open and the slightly more closed conformers of CTD, respectively; complexes without a dot represent a strongly bound state). This is followed by a rapid collision complex formation of two Zn^{2+} ions binding to the peripheral sites followed by an additional isomerization reflected by formation of a high fluorescence state termed 'compact closed' (CTD^{CC}, Figure 9). The microscopic rate constants are global binding parameters that reflect binding to both peripheral sites since we cannot distinguish between the two (Scheme 1). The observed rate constant (k_{obs}) of Zn^{2+} binding to WT exhibits a hyperbolic-dependence on Zn^{2+} concentration (Figure 8D). Based on the kinetic Scheme 1, and under the assumption that $k_{+\mathrm{ps}}[Zn^{2+}], k_{-\mathrm{ps}} >> k_{+\mathrm{ps}}^{\mathrm{CC}}$ ($K_{\mathrm{PS}} = k_{-\mathrm{ps}}/k_{+\mathrm{ps}}$), the observed rate constant for Zn^{2+} binding is predicted to follow a rectangular hyperbola and can be fitted accordingly to Equation 1:

$$k_{\mathrm{obs}} = \left(\frac{K_{\mathrm{PS}} \cdot k_{+\mathrm{ps}}^{\mathrm{CC}}[\mathrm{Zn}^{2+}]}{1 + K_{\mathrm{PS}}[\mathrm{Zn}^{2+}]} \right) + k_{\text{-ps}}^{\mathrm{CC}} \qquad \text{(Equation 1)}$$

Where K_{PS} represents the equilibrium constant for Zn^{2+} binding to the peripheral sites and $k_{+\mathrm{ps}}^{\mathrm{CC}}$ reflects the isomerization rate constant suggesting further closure of the CTD central cleft. The best fit of Zn^{2+} concentration-dependence binding to the WT according to Eq. 1 yields an equilibrium constant $1/K_{PS}$ = 62.6 ± 13.0 μM and an isomerization rate constant of $k_{+\mathrm{ps}}^{\mathrm{CC}}$≈ of 39.2 ± 1.4 sec^{-1} (see all rate constants in Table 6). The intercept of the fit is indistinguishable from the origin; thus, Zn^{2+} binding is essentially irreversible ($k_{+\mathrm{ps}}^{\mathrm{CC}}$ >>$k_{-\mathrm{ps}}^{\mathrm{CC}}$ ~0), consistent with the results of slow Zn^{2+} dissociation kinetics (see below, Figure 8F). The apparent second order binding constant $1/K_{PS} \cdot k_{+\mathrm{ps}}^{\mathrm{CC}}$ = 0.63 ± 0.14 μM^{-1} sec^{-1}, is surprisingly slow in comparison to a small ligand such as a charged ion binding to a protein [5], suggesting that the reaction is not diffusion limited. Interestingly, dissociation kinetics of Zn^{2+} measured by mixing a pre-equilibrated WT·Zn^{2+} with excess of EDTA exhibited double exponentials (Figure 8F). The dissociation rate constants, $k_{diss,fast}$ = 2.4 ± 0.1 sec^{-1} and $k_{diss,slow}$ = 0.20 ± 0.07 sec^{-1} may reflect dissociation events from the two different Zn^{2+} binding sites, the peripheral sites and the central site. However, the fact that similar dissociation kinetics are seen with PS (Figure 8G) and with similar magnitudes to the WT, $k_{diss,fast}$ = 4.6 ± 0.1 sec^{-1} and $k_{diss,slow}$ = 0.46 ± 0.02 s^{-1}, that was determined to not bind Zn^{2+} in the central site by the PELDOR and ITC measurements, would suggest otherwise. Furthermore, the faster dissociation rates suggest

that PS binds Zn^{2+} with a different conformation at the peripheral sites. The intercept in Figure 8D is similar to the slower dissociation rate measured directly ($k_{-ps}^{CC} \sim 0$ & $k_{diss,slow} = 0.20 \pm 0.07$ sec^{-1}, see Table 6) favoring a slower isomerization occurring before complete dissociation. Both WT and PS dissociation kinetics demonstrate that structurally the peripheral sites exchange Zn^{2+} with EDTA which can compete over the coordination of Zn^{2+} at these sites. Along with these arguments, we favor a two-step dissociation kinetic from the peripheral sites.

The amplitudes of the peripheral sites' binding kinetics are related to the fractional bound Zn^{2+}, and therefore to their overall affinity. Since these amplitudes report binding of two ligands to two identical sites, we utilized a simple Hill model. The fitting of the amplitudes for the WT according to Equation 2 is shown in Figure 8E with a $K_{H,WT}$ = 33.9 ± 1.3 μM and a moderate Hill coefficient $n_{H,WT}$= 1.61 ± 0.13 (Table 6).

$$A = \frac{V_{\max} \cdot [Zn^{2+}]^n}{K_H^n + [Zn^{2+}]^n} \qquad \text{(Equation 2)}$$

Comparison of the equilibrium constant measured by ITC for WT (K_d = 31.5 ± 3.4 μM, Table 5) with the equilibrium constant determined by the Hill model suggests that the overall affinities of both the central site and peripheral sites in the WT protein are only marginally different, though their kinetics seems to be on a very different time scale. This further agrees with the rapid dissociation from the central site as the 'on rate' is also very fast. This is not to classify them as similar in terms of their binding kinetic pathways and the impact of their binding on the allostery they may induce on each other.

Although PS displays a similar single-phase behavior (Figure 8B), with fluorescence increase upon Zn^{2+} binding, the k_{obs} dependence on Zn^{2+} concentration decreases rather than increases (Figure 8D, Table 6). Therefore, it may be that PS exhibits a different mechanism for Zn^{2+} peripheral site-binding than WT. In PS the fast binding step to the central site does not occur in the dead time as it does for WT. This is also evidenced by the PELDOR and ITC results which reveal a lower stoichiometry of Zn^{2+} binding to PS (Table 5, N = 2 and N = 2.41 ± 0.24 respectively), most likely only to the peripheral sites. This behavior is well-matched with a slower step of 'close' to 'open' conformational change preceding the metal ligand binding step to a 'selected conformation' (open state) [28]. The presence of an additional isomerization following the fast ligand binding step $CTD_{CSM}^{SC} \cdot (Zn^{2+})_2$ is not justified based on this hyperbolic Zn^{2+}-concentration-dependence of the k_{obs} (see below), as this may occur too fast to be detected. When we consider the dissociation kinetics of PS, the presence of an isomerization step $CTD_{CSM}^{SC}(Zn^{2+})_2$ as observed for the WT before the peripheral Zn^{2+} completely dissociated may be justified. This two-step dissociation most likely originates from a tighter complex, similar to the WT but albeit different structurally. Therefore, we propose the reaction mechanism in Scheme 2 for Zn^{2+} binding to PS stringently based on the observable 'on' rate. CTD_{CSM}^{SO} and CTD_{CSM}^{SC}

are the 'swivel open' and 'swivel closed' conformers of the PS CTD, respectively where CTD_{CSM}^{SCC} is the 'swivel compact closed' state (CSM for central site mutant represents the PS construct, so as to avoid confusion with the PS used to represent the peripheral sites in all the kinetic schemes) (Figure 9). At lower Zn^{2+} concentration, the binding of Zn^{2+} is limited by the presence of CTD_{CSM}^{SC} and hence the transition from CTD_{CSM}^{SO} to CTD_{CSM}^{SC} contributes to k_{obs}. At very high Zn^{2+} concentration the formation of $CTD_{CSM}^{SC} \cdot (Zn^{2+})_2$ is fast and k_{obs} is dominated by k_{+csm}^{s} ($K_{CSM}^{S} = k_{+csm}^{s} / k_{-csm}^{s}$) and will approach the net rate constant of this isomerization step. We further reason that the binding steps are faster than isomerization based on the relatively slow dissociation kinetics and the high affinity binding of Zn^{2+} to the mutant (ITC results, Table 5), hence at high Zn^{2+} concentration, $k_{+csm}^{s} \ll k_{+csm}^{ps}[Zn^{2+}]$ ($K_{PS} = k_{-csm}^{ps}/k_{+csm}^{ps}$). Therefore, in accordance with such a mechanism, Equation 3 can predict such an hyperbolic dependence on the Zn^{2+} concentration of decreasing observed rate constant (see Appendix S1 for the derivation of Equation 3 for this kinetic model, based on [29]):

$$k_{obs} = k_{+csm}^{s} + k_{-csm}^{s}\left(\frac{K_{CSM}^{PS}}{K_{CSM}^{PS} + [Zn^{2+}]}\right) \qquad \text{(Equation 3)}$$

We note that at lower concentration ($[Zn^{2+}] < 40$ μM) the transients of PS were not sufficiently qualitative with respect of signal to noise to attain good fitting while keeping peripheral sites under pseudo-first order reaction conditions and getting a reasonable fluorescence intensity. Therefore, fits were performed in the range of $[Zn^{2+}] > 40$ μM (Figure 8D, Table 6). This does not, however, change the assumption leading to the above mechanism. The 'swivel open' transition to 'swivel closed' is relatively fast (Table 6, k_{+csm}^{s} = 29.4 ± 1.6 sec^{-1}), but slower than the actual binding, reflecting the lack of steric repulsions in the structure. Interestingly, the dynamics between the swivel open and swivel closed conformations within PS are much more apparent in solution as revealed by the kinetics and MD than observed by the structural studies, emphasizing the benefits of such measurements. The equilibrium constants indicate that the swivel open conformation is only slightly more favorable than the swivel closed (K_{CSM}^{S} = 0.45 ± 0.27). The amplitudes determined from Zn^{2+} binding to PS (Figure 8E) produce a $K_{H,CSM}$ = 39.5 ± 2.2 μM but a stronger Hill coefficient n_H = 2.1 ± 0.2 (fitted to the range of Amp increase, Table 6). The loss of amplitudes at higher Zn^{2+} concentration is due to the loss of the fast component in the binding reaction where the 'swiveling' isomerization dominates the amplitude. The larger Hill coefficient suggests that the closure of the protomers by binding at the central site before binding at the peripheral sites occurs, is key to increase allostery in the peripheral sites.

Discussion

A new mode of metal binding to MamM CTD

The major impact of this work is the underlying mechanism of Zn^{2+} binding to MamM CTD via three putative metal binding sites. Taken together, these results, in terms of structure, thermodynamics and kinetics, suggest a model in which one Zn^{2+} ion readily binds, with fast kinetics, minimal energetic cost and very minor conformational changes to the central site. The ion binding changes the electrostatic properties of the binding cleft, which may however have a long-range effect on the peripheral sites as discussed below. This is followed by binding of an additional two Zn^{2+} ions, most likely simultaneously within the time regime of msec, to the peripheral sites, with slower kinetics as compared to the central site binding, at a larger energetic cost and with major conformational changes (Figure 9). Several lines of evidence are provided by using multiple approaches and dissection of site-specific mutant data in comparison to the WT. The PS and the CS constructs each provide separate but limited contributions to the overall mechanism since not everything can be experimentally measured with the perturbation of the central and the peripheral binding sites, respectively. The PS mutant provides a unique insight into the flexibility of the dimerization domain between the two monomers. When binding to the peripheral sites occurs, it seems that at very high Zn^{2+} concentration, a decrease in the observable rate is also associated with a decrease in the fluorescence intensity which may reflect intermolecular swiveling of the monomer similar but quite not identical to WT. So, in other words, the two domains are able to swivel along a perpendicular axis (Figure 9), as was proposed, but not experimentally demonstrated, previously [13]. In addition, in the PS mutant, the Hill coefficient was determined from the amplitudes of Zn^{2+} binding kinetics which points to the central site's tight closure contributing to an increase in allostery of Zn^{2+} peripheral site binding in comparison to the WT.

Fast Zn^{2+} binding to the central site has no energetic cost and facilitates the binding to the peripheral site

CS reveals no heat capacity change in the ITC binding experiments within the same range of Zn^{2+} concentration as for WT and PS, suggesting that binding to the central site occurs with only minor conformational changes. Zn^{2+} binding in CS also results in a minor fluorescence spectral shift yet a large increase in the fluorescence intensity. The PELDOR results suggest that although exhibiting a different distance range as compared to the apo form, the CS does not adopt a closed, distinct conformation when Zn^{2+} is added. In CS, it is more probable that entropy decreases due to the more ordered zinc ions bound at the central site. Furthermore, enthalpy is also slightly decreased, in a way that leads to nearly no net overall change in the Gibbs free energy of the system. This is further supported by the WT and PS ITC results which indicate that in equilibrium their energetic parameters

are very similar. As their final states are expected to be similar, binding to the central site does not contribute much to the overall heat change of the system. In terms of structural changes, one Zn^{2+} binds initially to the central site residues of only one monomer (nonspecifically), which occurs very fast (<1.5 msec, as resolved from the WT kinetic results). The binding of one such ion could potentially change the local electrostatic surface, driving the second monomer to close the binding site thus neutralizing the positive charge. Our results, however, indicate that binding at the central site only leads to minor conformational changes and the protein remains in a dynamic, open state. This is only altered when the peripheral sites are occupied, leading to the tighter, locked state (Figure 9), as evidenced from the PS and WT fluorescence and PELDOR results.

PS exhibits a different initial conformation and [Zn^{2+}]-dependent movement as compared to WT

The N value derived from ITC experiments of the WT and the PS mutants reflects the number of bound Zn^{2+} ions. These N values that were calculated from the ITC data indicate that the peripheral sites bind two ions (N_{PS} = 2.4), hence the central site populates only one Zn^{2+} ion (N_{WT} = 2.8, N_{CS} could not be calculated), which is lower than previous published results (N_{WT}=4) [13]. PS exhibits a slightly lower N than WT, however, it has a twofold tighter K_D than WT (lower ΔG), suggesting that the binding occupies less sites but with a tighter affinity. This can also be inferred from the PELDOR results where both a less dynamic conformation and/or a shorter smaller distance distribution for the apo PS is observed as compared with the apo WT, as well as a reduction in the number of bound Zn^{2+} ions. Structurally, this can be reasoned by a swiveling movement of the PS dimer (relative to the dimerization interface at the bottom of the V-shape) (Figure 9). Hence, and as was supported by the MD results, PS adopts a scissor-like conformation instead WT's V-shape apo conformation. This would suggest that the initial states of the two apo forms are different and hence their binding mechanism is different. In the final state both WT and PS involve the binding of Zn^{2+} in the two peripheral sites and adopt a more similar conformation as compared to their initial states, which is supported by both the fluorescence and PELDOR results. These different initial states are not reflected in crystal structure models of the apo forms which are likely restrained by crystal contacts. Further, the only apo crystal structure which could not be detected is that of PS-C267S, further supporting that it might adopt a different conformation.

Comparison of MamM CTD metal binding sites and conformational changes to other CDF proteins' CTDs suggests a complex regulation mechanism in CDF proteins

A comparison of our results in the wider context of the whole CDF protein family in terms of the binding sites and conformational changes observed in this study reveal further significant structural insights within the known CDFs' CTDs bound structures (Figure 10A). The evolutionary-closest CDF CTD structure that was solved in a Zn^{2+}-bound state is of MamB, another iron transporter CDF protein from MTB [14] (Figure 10B). Zn^{2+} in the MamB structure is chelated by D247 (homologous

to D249 in MamM), H283 (homologous to H285 in MamM) and H245 (found in the same location as W247 in MamM) (Figure 10C). Since MamM and MamB CTD sequences are highly conserved [14,17], MamB's crystal structure strengthens the evidence for the ability of MamM's central site to bind metals. However, in MamB, no conformational changes have yet been detected in the metal-bound state compared the apo structure (Figure 10B). This could be due to two reasons: (1) Zn^{2+} was only soaked into the crystals after their formation [14], a method that may not invoke significant further conformational changes due to pre-existing strong crystal contacts. (2) The MamB structure does not involve Zn^{2+} binding at a peripheral site (which contains aspartate and threonine residues rather than the histidine and glutamate residues found in MamM), which has been shown here to induce such major conformational changes.

All other CDF structures that were solved are of bacterial Zn^{2+} transporters (Figure 10D). CzrB is the only CDF protein whose CTD structure has been solved in both the apo and bound-closed forms. CzrB structures exhibit much larger conformational change between the apo and the bound-closed states [12] when compared to the degree-of-closure indicated by the PELDOR results for MamM. Moreover, the metal binding sites are not completely conserved between MamM and CzrB. The peripheral site of MamM involves H264 from one monomer and E289 from the other. In CzrB, one of the Zn^{2+} ions is chelated by homologous histidine and glutamate residues that are found in the same positions (H258 and E282), but also by an additional histidine (H280, homologous to S287 in MamM) (Figure 10E). Additionally, there are two Zn^{2+} ions bound per monomer in CzrB, that do not involve homologous residues to those of MamM binding sites and which involve residues only from one monomer (E243, homologous to D249 in MamM, is found at a distance of 3.71 Å from one of these ions, a long distance for an expected strong electrostatic interaction, therefore it is not expected to contribute much to the binding of the ion in this site). However, one of these Zn^{2+} ions (namely the second Zn^{2+} ion) is also bound by E282 and by other residues that are involved in the binding of the third Zn^{2+} [12] (Figure 10D), suggesting a net of Zn^{2+}-protein interactions that can lead to the stable binding of Zn^{2+} in the CzrB peripheral site. The first two Zn^{2+} ions discussed in the context of CzrB are also found in the same locations and are ligated by homologous residues in the bacterial CDF model protein YiiP, for which only its closed structure has been solved [9,10,30,31] (Figure 10D,E). Such a multiple-Zn^{2+}-binding state is not possible in MamM as some of the homologous residues in MamM are not suited to metal binding, yet despite this both the CzrB and YiiP closed structures support the importance of the peripheral site residues for metal binding and conformational changes, as revealed in this study.

The comparison between all CDFs CTDs' structures and binding sites reveals a complex regulatory mechanism for CDF proteins. The Zn^{2+} transporters show a network of Zn^{2+} binding sites that includes the peripheral sites and extends towards the center of the proteins, while the iron transporter MamB binds ion only in the center of the V-shaped dimer. MamM contains both the central and peripheral sites, suggesting a double-safe mechanism for this specific protein compared to MamB, and

a different regulation mechanism compared to the Zn^{2+} transporters: one site allows rapid binding and a change of the charge distribution, which facilitates the binding to the second site. This allows the conformational lock-down that will lead to further transmembrane domain conformational changes and active transport. Previous *in vivo* studies of MamM showed that mutations in both the central and peripheral CTD binding sites lead to small variations in magnetosome size, number and magnetic response [13]. These rather small changes might suggest that although the regulation is important for normal function, the transport can occur even when this regulation path is defected, meaning that metal can diffuse to the transmembrane domain independently, yet less efficiently. However, even mutations in the conserved transmembrane transport site of MamM, which were shown previously in many CDF proteins to have a drastic influence on the proteins' function, showed relatively small impact on magnetite formation [8,17]. Hence, we speculate that MamB somehow compensates MamM function as opposed to mutations in the CTD binding sites having only a minor impact on the protein function.

All the known CDF proteins' CTD structures support our key finding of the capability of the central site to bind metal readily without any further large conformational changes. In addition, binding to the peripheral sites affords the induction of conformational changes in the dimer. While the transmembrane transport site is conserved between the different CDF proteins (in terms of location and importance for function) which implies a similar transport mechanism [8,11], the apparent versatility in the binding sites and conformations between the proteins CTDs suggest diverse regulation mechanisms for different proteins. The fine tuning in the regulation might be evolution-related, since more highly evolved organisms emerge more sophisticated and complex regulation mechanisms. For example, recent studies of eukaryotic CDF proteins (plant MTP proteins and human ZnT proteins) suggest that other elements such as a His-rich loop - a cytoplasmatic loop between two transmembrane helices that is not found in the structurally-characterized CDF proteins - might play a role in protein regulation [32,33]. Further biochemical and structural studies of CDF proteins that are not Zn^{2+} or Fe^{2+} transporters proteins, and of eukaryotic CDF proteins, would be required to decipher the evolutionary pathway of the regulation mechanism in CDF proteins.

To conclude, the kinetics of the transport rate of the full length CDF protein has been previously studied by the detection of change in Zn^{2+} concentration inside a vesicle. Here for the first time the conformational dynamics and kinetics of the CTD upon Zn^{2+} binding have been directly studied, revealing a molecular mechanism for binding, including stoichiometry, allostery, energetics and the order of binding. The structure-function relationships revealed here demonstrate how metal binding to a CTD of a CDF protein leads to distinct conformational changes within this domain in solution, thus significantly strengthening previous evidence highlighting the importance of CTD for overall protein regulation and function.

Materials and Methods

Site-directed mutagenesis and protein expression. *mamM* CTD gene (UniProt Q6NE57 residues 215-318) was previously cloned into pET28a(+) vector (Novagen, Merck Biosciences, Darmstadt, Germany) [34]; in this construct, pET28a-MamM-CTD-MSR1, the *mamM* gene was fused in-frame to express a six-His tag at the N-terminus of the protein followed by a thrombin proteolysis site. All MamM CTD mutations were applied to the pET28a-MamM-CTD-MSR1 vector using the QuickChange site-directed mutagenesis method (Stratagene, La Jolla, CA, USA). Primers containing single mutation sites (Hylabs, Rehovot, Israel) were designed and used for PCR amplifications. All MamM CTD forms were expressed similarly to previously described for MamM CTD WT [34]: *E. coli* Rosetta(DE3)pLysS strain cells (Novagen) harboring the pET28a-MamM-CTD-MSR1 plasmid were grown in auto-induction medium [35] containing kanamycin (100 mg mL^{-1}) and chloramphenicol (30 mg mL^{-1}) at 310 K for 6 hours. The cultivation temperature was then reduced from 310 to 300 K for a further 18 hours. The cells were harvested by centrifugation at 7438g for 8 min at 277 K.

Protein purification. All proteins used in this study were purified similarly to previously described for MamM CTD M250L mutant [19,34]. All MamM CTD forms expressing cells were suspended in binding buffer containing 50 mM Tris-HCl pH=8, 300 mM NaCl, 20 mM imidazole, 5 mM β-mercaptoethanol and 0.01% Triton X-100 at a weight ratio of 1:2, with DNaseI (10 μg mL^{-1}) and a protease inhibitor cocktail (containing 100 μM phenylmethylsulfonyl fluoride (PMSF), 1.2 μg mL^{-1} leupeptin and 1 μM pepstatin A) for 30 min at 277 K. The cells were then disrupted by three cycles of French press pressure cell (Thermo Scientific, Waltham, MA, USA) at 207 MPa. Cell debris was separated by centrifugation at 45,000 RPM (60 Ti fixed angle rotor, Beckman Coulter, Brea, CA, USA) for 45 min at 277 K and the soluble fraction was applied onto a home-made gravity Ni-NTA column (2.5 cm diameter Econo-Column by Bio-Rad, Hercules, CA, USA; 5 mL bed volume of HisPur Ni-NTA resin by Thermo Scientific) pre-equilibrated with the binding buffer. Protein were washed with 50 mL of two washing buffers for further purification, containing: (1) 20 mM Tris-HCl pH=8, 1 M NaCl, 40 mM imidazole and 5 mM β-mercaptoethanol, (2) 20 mM Tris-HCl pH=8, 150 mM NaCl, 40 mM imidazole and 5 mM β-mercaptoethanol, and eluted with buffer containing 20 mM Tris-HCl pH=8, 150 mM NaCl, 500 mM imidazole and 5 mM β-mercaptoethanol. To remove the six-His tag, bovine thrombin (10 U mL^{-1}; t4648-10KU, Sigma-Aldrich, St. Louis, MO, USA) was added to the eluted protein and the mixture dialyzed against the final buffer, containing 10 mM Tris-HCl pH=8, 150 mM NaCl and 5 mM β-mercaptoethanol for 16 hours at 277 K. Protein was then concentrated to a volume of 4 mL using a Vivaspin-4 (3000 Da MW cutoff; Sartorius Stedim Biotech GmbH, Goettingen, Germany) and applied onto a size-exclusion column (HiLoad 26/60 Superdex 75;

GE Healthcare Biosciences, Danyel Biotech Ltd., Rehovot, Israel) pre-equilibrated with the final buffer. Selected peaks of pure protein were collected and concentrated using a Vivaspin-4 to a final concentration of 10-60 mg mL^{-1}, flash-frozen in liquid nitrogen and stored at 193 K for further use. Throughout the purification process, protein concentration was determined by measuring absorption at 280 nm, and protein purity was analyzed by SDS-polyacrylamide gel electrophoresis (PAGE). For all C267S constructs, β-mercaptoethanol was not used during purification and in the final storage solutions. For all further experiments, protein concentration was also determined by measuring absorption at 280 nm.

Crystallization and structure determination. Purified MamM CTD proteins: W247A in buffer containing 10 mM Tris pH=8.0, 150 mM NaCl, and 5 mM β-mercaptoethanol; CS in buffer containing 10 mM Tris pH=8.0, 150 mM NaCl, 3.375 mM $MnCl_2$ and 5 mM β-mercaptoethanol; CS-C267S and C267S in buffer containing 10 mM Tris pH=8.0, 150 mM NaCl (buffer A); were crystallized using the vapor diffusion method at 293 K (0.3 μL protein with a 0.3 μL reservoir solution for all proteins but CS, where 1 μL protein with 1 μL reservoir solution were used). Crystals were harvested with or without treatment of cryo agent and flash-frozen in liquid nitrogen. Data collection was performed on a single-crystal at a temperature of 100 K. All cryo conditions, data collection details, data reduction and scaling, phasing and refinement details are given in Tables 1-3.

Least-squares overlaps. MamM CTD structures were overlaid and RMSDs calculated using the iterative magic fit tool of Swiss-PdbViewer 4.1.0 [36]. All MamM CTD structures and all overlapped structure figures were prepared using UCSF Chimera package, version 1.12 [37].

Circular dichroism measurements. CD measurements were performed using a J750 spectropolarimeter (Jasco Inc, Easton, MD, USA) at ambient temperature. MamM CTD proteins were incubated with EDTA for 5 hours, which was subsequently removed by dialysis. The proteins were diluted to a final concentration of 0.3 mg mL^{-1}, with or without Zn^{2+} (15:1 Zn^{2+} to protein ratio), in a buffer containing 10 mM Tris-HCl pH=8, 50 mM NaCl and 0.188 mM β-mercaptoethanol, and measured with a 0.1 cm optical path Suprasil quartz cuvette (Hellma GmbH & Co., Müllheim, Germany). Spectra profiles of the samples were measured in a wavelength range of 200-260 nm, with a bandwidth of 1 nm, a scan speed of 5 nm min^{-1} and a time constant of 8 sec.

Site-directed spin labelling. For site-directed spin labelling, protein solutions in buffer A (containing 10 mM Tris-HCl pH=8 and 150 mM NaCl) were degassed under argon and treated with degassed 1,4-Dithiotheitol (DTT, 1 mM) for 4 hours at 4 ^{o}C with gentle agitation. Subsequently, protein samples were washed once using Zeba^{TM} Spin desalting columns (7 kDa MWCO, 2 mL; Thermo ScientificFisher, Waltham, MA, USA) and degassed buffer A. Protein was then labelled overnight at 4 ^{o}C with (1-oxyl-2,2,5,5-tetramethylpyrrolidin-3-yl)methylthiosulfonate spin label (MTSL, 20x excess) (Toronto Research Chemicals Inc., North York, Ontario, Canada) under gentle agitation. To remove excess unbound MTSL, samples were washed twice using Zeba^{TM} Spin desalting Columns and degassed buffer A.

Pulsed electron-electron double resonance measurements. Spin-labelled variants were lyophilised before being taken up in D_2O to a final concentration of 150-200 μM, and EPR samples (both apo and Zn^{2+}-containing) were prepared with 30 % Glycerol-d_8 (Sigma-Aldrich). For Zn^{2+}-containing samples, $ZnCl_2$ stock solutions were prepared in buffer A (in D_2O). Each spin-labelled variant C267S, PS-C267S and CS-C267S was incubated with a 5-fold excess of Zn^{2+} for 1 hour at room temperature, then Glycerol-d_8 was added. A 100 μL sample was loaded into an EPR quartz tube (Wilmad SQ-707; Wilmad-LabGlass, Vinland, NJ, USA) and flash frozen in liquid nitrogen. For the titration experiment of the C267S variant, the previously measured apo sample was first thawed slowly over liquid-N_2 and removed from its EPR tube to an eppendorf. Zn^{2+} was then added (1x excess) and the sample was allowed to incubate at room temperature for approximately 2 hours before transferring back into the tube, flash freezing and re-measuring. This was repeated for Zn^{2+} excesses of 2x, 3x, 4x, 5x, 6x, 8x, and 10x using the same sample. The same experimental approach was taken for the titration experiment of the PS-C267S variant, this time with Zn^{2+} excesses of 1x, 2x, 3x and 5x. X-band pulsed EPR spectra were recorded on a Bruker E580 spectrometer (Bruker, Rheinstetten, Germany) using a Bruker MD5-W1 EPR probehead equipped with a self-modified cryogen-free cryostat (Advanced Research Systems Inc, Macungie, PA, USA). The microwave pulses were amplified using a 1kW-TWT (Applied Systems Engineering Inc., Fort Worth, TX, USA). All EPR experiments were carried out at 60K. The field-swept spectrum was obtained by integrating the Hahn echo signal as a function of the magnetic field after a two-pulse sequence.

For the 4-pulse PELDOR experiments recorded at 60 K, pulse lengths were 20 nsec for $\pi/2$ and 20 nsec for π. The pump pulse length was 16 nsec and $\Delta\nu$ ($\nu_{obs} - \nu_{pump}$) was 70 MHz. The pulse separation τ_1 was 352 nsec (C267S apo), 386 nsec (CS-C267S apo) or 120 nsec (all others), while τ_2 varied between 2000-4000 ns, and the echo signals were integrated using a video amplifier bandwidth of 20 MHz. The pump pulse was stepped out by 16 nsec for a total number of points in T that depended

upon the τ_2 used. Nuclear modulation artifacts were suppressed using a systematic variation of the interpulse delay time τ_1 and an appropriate phase cycling routine.

Molecular dynamics and principal component analysis. All MD simulations were performed using the NAMD molecular dynamics software version 2.13b2 [38]. The CHARMM 36/CMAP force field [39] with TIP3P water model [40] was used to describe the system.

During simulations, a time step of 2 fsec was used. In all simulations, periodic boundary conditions with the particle mesh Ewald algorithm for electrostatics were employed [41]. All simulations were performed under the same conditions: temperature was held constant using Langevin dynamics at 300 K with a damping coefficient, 1 $psec^{-1}$; pressure was held constant using Langevin piston method at 1 atm also with a damping coefficient, 1 $psec^{-1}$, piston's oscillation period to 100 fsec and pistons decay time of 50 fsec; switching and cutoff distances, 1 nm and 1.2 nm, respectively; pairlist distance, 1.4 nm.

System preparation was done using the VMD software package version 1.93 [42]. Initial models of WT and PS were based on the PDB IDs: **3W5X** and **3W66**, respectively [13]. All simulated proteins were solvated into a water box with a minimum solvation shell of 14 Å thickness. Simulated systems were then neutralized by adding counter ions at random positions. Before initiating free MD simulations, all systems were minimized and equilibrated. Initially, each system was submitted to 10K steps of conjugate gradient minimization where protein's heavy atoms are positionally restrained. This minimization was followed by two steps of equilibration. First, each system was heated to 300 K while simulated for 200 psec under NVT conditions with the solute's heavy atoms restrained. Secondly, each system was simulated using the NPT ensemble for 200 nsec while restraints are gradually removed. Finally, each system was submitted to free NPT 200 nsec length MD simulations.

Analyses were performed using GROMACS version 2018.1 [43]. Analyses were performed on the productive stage of the simulations (i.e. after the first 20 nsec). For the root mean square deviation (RMSD) analysis, the positional deviations of backbone heavy atoms (N, Cα, C), with respect to their initial structure, were calculated every 10 psec (after performing a least square fit to their initial structure). For fluctuation profile analysis, fluctuations of backbone heavy atoms (N, Cα, C and O) with respect to their initial structure were calculated every 10 psec (after performing a least square fit to their initial structure).

All visualization was done using the PyMOL Molecular Graphics System, Version 2.3 (Schrödinger, LLC.). Principle movements were drawn using the *modevectors.py* script by Sean M. Law.

Isothermal titration calorimetry measurements and analysis. ITC measurements were performed in low-volume Nano ITC calorimeter (TA Instruments, New Castle, DE, USA) at 298 K. Proteins were prepared in buffer A and Zn^{2+} solutions in buffer containing 1 mM Tris pH=8 and 150 mM NaCl. All proteins were diluted to 50 µM and titrated with: Zn^{2+} 1.4 mM (WT), Zn^{2+} 1 mM (PS) or Zn^{2+} 750 µM (CS). The protein samples were injected into the instrument cell (170 µL) and 20 aliquots of 2.5 µL of a suitable $ZnCl_2$ solution were titrated into the cell every 350 seconds. For each protein, 3 independent titrations were recorded. As a control, each $ZnCl_2$ solution was also titrated into buffer A under identical experimental conditions, and all measurements were compared to a Double-distilled water-containing reference cell. Data were analyzed using TA NanoAnalyze Data Analysis software, version 3.7.5 (TA Instruments, New Castle, DE, USA). For WT and PS, data for each measurement was fitted after reduction of the control to an independent model combined with a blank constant model, and the thermodynamics values determined are the average of three different titrations for each protein. Errors are reported as the standard deviation.

Fluorescence spectrometry measurements and analysis. Changes in tryptophan intrinsic fluorescence were monitored using a Fluorolog®-3 (HORIBA Scientific, Edison, NJ, USA) equipped with 1cm optical path length quartz cell at ambient temperature. 1mL samples MamM CTD proteins at 5 µM in buffer A were titrated using a 1 mM $ZnCl_2$ solution in the same buffer to reach different Zn^{2+} concentrations. Samples were measured at an excitation of λ_{ex} 297 nm, and the emission spectrum for each Zn^{2+} concentration recorded between 310-450 nm. Each protein-metal titration was replicated three times, and each spectrum was fitted to an extreme function using OriginPro (R-Square (COD) > 0.98) (OriginLab Corporation, Northampton, MA, USA). The maximum wavelength (wavelength of maximum intensity) and the intensity at that wavelength (aka maximum intensity) were averaged for each Zn^{2+} concentration. Errors are reported as the standard deviation.

Stopped-flow measurements and analysis. Stopped flow experiments were performed using a temperature-controlled Tech Scientific SF-61DX2 stopped-flow instrument (TgK Scientific Ltd., Bradford-on-Avon, UK) at 298 K. All proteins, Zn^{2+} and EDTA solutions were prepared in buffer A. Proteins at 5 µM initial concentration were injected at a 1:1 ratio with Zn^{2+} solutions (40-460 µM initial concentrations for WT, 30-460 µM initial concentrations for PS) into the 20 µL reaction cell.

For the dissociation experiment, protein at 5 µM pre-equilibrated with 300 µM Zn^{2+} was injected in a 1:1 ratio with 2 mM / 5 mM EDTA solutions (initial concentrations) into the 20 µL reaction cell. Samples were excited at λ_{ex} 297 nm and the tryptophan fluorescence signal was recorded through a long-pass 320 nm filter. For each injection, 2000 data points were collected for 10 sec at logarithmic time scale containing 10 cycles of 200 points/cycle.

For the association measurements of MamM CTD with Zn^{2+} n=2 was used, while for the dissociation measurements of the MamM CTD - Zn^{2+} with EDTA n=1 was used, where n is the number of independent measurements (different protein and Zn^{2+} stocks and initialized instrument; in each measurement of protein-Zn^{2+} or protein-Zn^{2+}-EDTA ratio, at least three injections were averaged). Data were averaged and analyzed using the Kinetic Studio software provided with the instrument or with OriginPro. Time-dependent changes of the fluorescence signal were fitted to the exponential function given in Equation 4:

$$F(t) = F_{\infty} + \sum_{i=1}^{n} A_i \cdot e^{-k_i t} \qquad \text{(Equation 4)}$$

Where *F(t)* is the fluorescence signal at time *t*, F_{∞} is the signal at t_{10sec}, A_i is the amplitude, k_i is the observed rate constant, *i* represents the i^{th} relaxation processes, and *n* is the total number of relaxation processes, which is either 1 (for a single exponential, e.g. for PS and WT) or 2 (for a double exponential, dissociation experiments). Data were fitted in the time range 1.5 - 200 msec for PS or 1.5 - 500 msec for WT for a single exponential, or in time range of 0.0015 - 10 sec for the double exponential EDTA experiments, to exclude the continuous-flow phase of mixing and the tryptophan photobleaching phase.

Author Contributions

All authors designed the study, analyzed the results and wrote the paper. SBZ and JH conducted the experiments, IK performed the MD simulations and MVS assisted with kinetic modeling. All authors approved the final version of the manuscript.

Acknowledgments

We thank Dr. Anat Shahar for her help with the crystallographic data collection and analysis, to Dr. Tamar Kurzion-Zilbermann for her assistance in CD measurements, to Geula Davidov and to Dr. Nitzan Kutnowski for their help with the ITC measurements and to Prof. Ofer Yifrach for fruitful discussion. SBZ and RZ are supported by the Israel Ministry of Science, Technology and Space; the Israel Science Foundation (grant no. 167/16); the European Molecular Biology Organization and the

EU (CMST COST Action CM1306 Understanding Movement and Mechanism in Molecular Machines). This work was supported in part by the Royal Society (FM was a Wolfson Research Merit Award Holder); the EU (COST Action CM1306 Understanding Movement and Mechanism in Molecular Machines) to FM. JH was supported by the BBSRC Norwich Research Park Biosciences Doctoral Training Partnership grant number BB/M011216/1. AH and MVS are supported by the Israel Science Foundation (grants 296/13) and Marie Curie Career Integration Award to AH (grants 1403705/11). Finally, we thank Geffen Zucker for being an integral part of this work and influencing every part of it.

References

1 Laity JH, Lee BM & Wright PE (2001) Zinc finger proteins: new insights into structural and functional diversity. *Curr Opin Struct Biol* 11, 39–46.

2 Cox N, Retegan M, Neese F, Pantazis DA, Boussac A & Lubitz W (2014) Photosynthesis. Electronic structure of the oxygen-evolving complex in photosystem II prior to O-O bond formation. *Science* 345, 804–808.

3 Kanteev M, Goldfeder M & Fishman A (2015) Structure-function correlations in tyrosinases. *Protein Sci* 24, 1360–1369.

4 Dupureur CM (2008) Roles of metal ions in nucleases. *Curr Opin Chem Biol* 12, 250–255.

5 Berg OG & von Hippel PH (1985) Diffusion-controlled macromolecular interactions. *Annu Rev Biophys Biophys Chem* 14, 131–160.

6 Dudev T & Lim C (2014) Competition among Metal Ions for Protein Binding Sites: Determinants of Metal Ion Selectivity in Proteins. *Chem Rev* 114, 538–556.

7 Montanini B, Blaudez D, Jeandroz S, Sanders D & Chalot M (2007) Phylogenetic and functional analysis of the Cation Diffusion Facilitator (CDF) family: improved signature and prediction of substrate specificity. *BMC Genomics* 8, 107.

8 Kolaj-Robin O, Russell D, Hayes K a., Pembroke JT & Soulimane T (2015) Cation Diffusion Facilitator family: Structure and function. *FEBS Lett* 589, 1283–1295.

9 Lu M, Chai J & Fu D (2009) Structural basis for autoregulation of the zinc transporter YiiP. *Nat Struct Mol Biol* 16, 1063–1067.

10 Lopez-Redondo ML, Coudray N, Zhang Z, Alexopoulos J & Stokes DL (2018) Structural basis for

the alternating access mechanism of the cation diffusion facilitator YiiP. *Proc Natl Acad Sci* 115, 3042–3047.

11 Barber-Zucker S, Shaanan B & Zarivach R (2017) Transition metal binding selectivity in proteins and its correlation with the phylogenomic classification of the cation diffusion facilitator protein family. *Sci Rep* **7**, 16381.

12 Cherezov V, Höfer N, Szebenyi DME, Kolaj O, Wall JG, Gillilan R, Srinivasan V, Jaroniec CP & Caffrey M (2008) Insights into the mode of action of a putative zinc transporter CzrB in Thermus thermophilus. *Structure* 16, 1378–1388.

13 Zeytuni N, Uebe R, Maes M, Davidov G, Baram M, Raschdorf O, Nadav-Tsubery M, Kolusheva S, Bitton R, Goobes G, Friedler A, Miller Y, Schüler D & Zarivach R (2014) Cation diffusion facilitators transport initiation and regulation is mediated by cation induced conformational changes of the cytoplasmic domain. *PLoS One* 9, e92141.

14 Uebe R, Keren-Khadmy N, Zeytuni N, Katzmann E, Navon Y, Davidov G, Bitton R, Plitzko JM, Schüler D & Zarivach R (2018) The dual role of MamB in magnetosome membrane assembly and magnetite biomineralization. *Mol Microbiol* 107, 542–557.

15 Barber-Zucker S & Zarivach R (2017) A Look into the Biochemistry of Magnetosome Biosynthesis in Magnetotactic Bacteria. *ACS Chem Biol* 12, 13–22.

16 Uebe R & Schüler D (2016) Magnetosome biogenesis in magnetotactic bacteria. *Nat Rev Microbiol* 14, 621–637.

17 Uebe R, Junge K, Henn V, Poxleitner G, Katzmann E, Plitzko JM, Zarivach R, Kasama T, Wanner G, Pósfai M, Böttger L, Matzanke B & Schüler D (2011) The cation diffusion facilitator proteins MamB and MamM of *Magnetospirillum gryphiswaldense* have distinct and complex functions, and are involved in magnetite biomineralization and magnetosome membrane assembly. *Mol Microbiol* 82, 818–835.

18 Zeytuni N, Uebe R, Maes M, Davidov G, Baram M, Raschdorf O, Friedler A, Miller Y, Schüler D & Zarivach R (2014) Bacterial magnetosome biomineralization-a novel platform to study molecular mechanisms of human CDF-related Type-II diabetes. *PLoS One* 9, e97154.

19 Barber-Zucker S, Uebe R, Davidov G, Navon Y, Sherf D, Chill JH, Kass I, Bitton R, Schüler D & Zarivach R (2016) Disease-Homologous Mutation in the Cation Diffusion Facilitator Protein MamM Causes Single-Domain Structural Loss and Signifies Its Importance. *Sci Rep* 6, 31933.

20 Jeschke G (2016) Dipolar Spectroscopy - Double-Resonance Methods. In *eMagRes* (Ashbrook S),

pp. 1459–1476. John Wiley & Sons, Ltd, Chichester, UK.

21 Jeschke G (2012) DEER Distance Measurements on Proteins. *Annu Rev Phys Chem* 63, 419–446.

22 Jeschke G (2018) MMM: A toolbox for integrative structure modeling. *Protein Sci* 27, 76–85.

23 Jeschke G, Chechik V, Ionita P, Godt A, Zimmermann H, Banham J, Timmel CR, Hilger D & Jung H (2006) DeerAnalysis2006—a comprehensive software package for analyzing pulsed ELDOR data. *Appl Magn Reson* 30, 473–498.

24 David CC & Jacobs DJ (2014) Principal Component Analysis: A Method for Determining the Essential Dynamics of Proteins. In *Methods in molecular biology* (Livesay D, ed), pp. 193–226. Humana Press, Totowa, NJ.

25 Ichiye T & Karplus M (1991) Collective motions in proteins: A covariance analysis of atomic fluctuations in molecular dynamics and normal mode simulations. *Proteins Struct Funct Genet* 11, 205–217.

26 Amadei A, Linssen ABM & Berendsen HJC (1993) Essential dynamics of proteins. *Proteins Struct Funct Genet* 17, 412–425.

27 Xiao Z & Wedd AG (2010) The challenges of determining metal–protein affinities. *Nat Prod Rep* 27, 768–789.

28 Fersht A (1999) Measurement and Magnitude of Individual Rate Constants. In *Structure and mechanism in protein science : a guide to enzyme catalysis and protein folding* (Hadler GL, ed), pp. 148–153. W.H. Freeman and Company, NY.

29 Hannemann DE, Cao W, Olivares AO, Robblee JP & De La Cruz EM (2005) Magnesium, ADP, and Actin Binding Linkage of Myosin V: Evidence for Multiple Myosin V−ADP and Actomyosin V−ADP States. *Biochemistry* 44, 8826–8840.

30 Coudray N, Valvo S, Hu M, Lasala R, Kim C, Vink M, Zhou M, Provasi D, Filizola M, Tao J, Fang J, Penczek P a, Ubarretxena-Belandia I & Stokes DL (2013) Inward-facing conformation of the zinc transporter YiiP revealed by cryoelectron microscopy. *Proc Natl Acad Sci U S A* 110, 2140–2145.

31 Lu M & Fu D (2007) Structure of the zinc transporter YiiP. *Science* 317, 1746–1748.

32 Fukue K, Itsumura N, Tsuji N, Nishino K, Nagao M, Narita H & Kambe T (2018) Evaluation of the roles of the cytosolic N-terminus and His-rich loop of ZnT proteins using ZnT-2 and ZnT-3 chimeric mutants. *Sci Rep* 8, 14084.

33 Tanaka N, Fujiwara T, Tomioka R, Krämer U, Kawachi M & Maeshima M (2015) Characterization of the histidine-rich loop of *arabidopsis* vacuolar membrane zinc transporter AtMTP1 as a sensor of zinc level in the cytosol. *Plant Cell Physiol* 56, 510–519.

34 Zeytuni N, Offer T, Davidov G & Zarivach R (2012) Crystallization and preliminary crystallographic analysis of the C-terminal domain of MamM, a magnetosome-associated protein from *Magnetospirillum gryphiswaldense* MSR-1. *Acta Crystallogr Sect F Struct Biol Cryst Commun* 68, 927–930.

35 Studier FW (2005) Protein production by auto-induction in high-density shaking cultures. *Protein Expr Purif* 41, 207–234.

36 Guex N & Peitsch MC (1997) SWISS-MODEL and the Swiss-PdbViewer: an environment for comparative protein modeling. *Electrophoresis* 18, 2714–2723.

37 Pettersen EF, Goddard TD, Huang CC, Couch GS, Greenblatt DM, Meng EC & Ferrin TE (2004) UCSF Chimera-A visualization system for exploratory research and analysis. *J Comput Chem* 25, 1605–1612.

38 Phillips JC, Braun R, Wang W, Gumbart J, Tajkhorshid E, Villa E, Chipot C, Skeel RD, Kalé L & Schulten K (2005) Scalable molecular dynamics with NAMD. *J Comput Chem* 26, 1781–1802.

39 Best RB, Zhu X, Shim J, Lopes PEM, Mittal J, Feig M & MacKerell AD (2012) Optimization of the Additive CHARMM All-Atom Protein Force Field Targeting Improved Sampling of the Backbone ϕ, ψ and Side-Chain χ_1 and χ_2 Dihedral Angles. *J Chem Theory Comput* 8, 3257–3273.

40 Jorgensen WL, Chandrasekhar J, Madura JD, Impey RW & Klein ML (1983) Comparison of simple potential functions for simulating liquid water. *J Chem Phys* 79, 926.

41 Essmann U, Perera L, Berkowitz ML, Darden T, Lee H & Pedersen LG (1995) A smooth particle mesh Ewald method. *J Chem Phys* 103, 8577–8593.

42 Humphrey W, Dalke A & Schulten K (1996) VMD: visual molecular dynamics. *J Mol Graph* 14, 33–38, 27–28.

43 Abraham MJ, Murtola T, Schulz R, Páll S, Smith JC, Hess B & Lindahl E (2015) GROMACS: High performance molecular simulations through multi-level parallelism from laptops to supercomputers. *SoftwareX* 1–2, 19–25.

44 Kabsch W (2010) XDS. *Acta Crystallogr D Biol Crystallogr* 66, 125–132.

45 Otwinowski Z & Minor W (1997) Processing of X-ray diffraction data collected in oscillation mode. *Methods Enzymol* 276, 307–326.

46 Evans PR & Murshudov GN (2013) How good are my data and what is the resolution? *Acta Crystallogr Sect D Biol Crystallogr* 69, 1204–1214.

47 McCoy AJ, Grosse-Kunstleve RW, Adams PD, Winn MD, Storoni LC & Read RJ (2007) Phaser crystallographic software. *J Appl Crystallogr* 40, 658–674..

48 Murshudov GN, Skubák P, Lebedev AA, Pannu NS, Steiner RA, Nicholls RA, Winn MD, Long F & Vagin AA (2011) REFMAC5 for the refinement of macromolecular crystal structures. *Acta Crystallogr D Biol Crystallogr* 67, 355–367.

49 Joosten RP, Long F, Murshudov GN & Perrakis A (2014) The PDB_REDO server for macromolecular structure model optimization. *IUCrJ* 1, 213–220.

50 Adams PD, Afonine P V, Bunkóczi G, Chen VB, Davis IW, Echols N, Headd JJ, Hung L-W, Kapral GJ, Grosse-Kunstleve RW, McCoy AJ, Moriarty NW, Oeffner R, Read RJ, Richardson DC, Richardson JS, Terwilliger TC & Zwart PH (2010) PHENIX: a comprehensive Python-based system for macromolecular structure solution. *Acta Crystallogr D Biol Crystallogr* 66, 213–221.

51 Emsley P, Lohkamp B, Scott WG & Cowtan K (2010) Features and development of Coot. *Acta Crystallogr D Biol Crystallogr* 66, 486–501.

52 Winn MD, Ballard CC, Cowtan KD, Dodson EJ, Emsley P, Evans PR, Keegan RM, Krissinel EB, Leslie AGW, McCoy A, McNicholas SJ, Murshudov GN, Pannu NS, Potterton EA, Powell HR, Read RJ, Vagin A & Wilson KS (2011) Overview of the CCP4 suite and current developments. *Acta Crystallogr D Biol Crystallogr* 67, 235–242.

Tables

Table 1: Crystallization of MamM CTD mutants.

Protein name	**MamM CTD C267S**	**MamM CTD W247A**	**MamM CTD H264A-E289A-C267S**	**MamM CTD H264A-E289A**
PDB ID	**6G55**	**6G6I**	**6G5E**	**6G64**
Crystallization conditions	0.2 M Li_2SO_4, 0.1 M BIS-TRIS pH=5.5, 25% PEG 3350	0.1 M BIS-TRIS pH=5.5, 20% PEG 3350	0.2 M Li_2SO_4, 0.1 M BIS-TRIS pH=5.5, 25% PEG 3350	0.2 M $(NH_4)_2SO_4$, 0.1 M BIS-TRIS pH=5.5, 22% PEG 3350
Cryo protectant	-	50% PEG 3350	-	-
Protein concentration (mg mL^{-1})	7.5	6.08	5	10
Crystallization type	Vapor diffusion sitting drop			
Data collection	P13 - DESY	ID29 - ESRF	ID29 - ESRF	Home source
Detector	Pilatus 6M	Pilatus 6M	Pilatus 69	MAR345

Table 2: Data collection and refinement statistics of MamM CTD mutants.

Protein name	**MamM CTD C267S**	**MamM CTD W247A**	**MamM CTD H264A-E289A-C267S**	**MamM CTD H264A-E289A**
PDB ID	**6G55**	**6G6I**	**6G5E**	**6G64**
Data collection	P13 - DESY	ID29 - ESRF	ID29 - ESRF	Home source
Space group	C 2 2 2_1	$P2_1$ 2_1 2_1	C2 2 2_1	C 2 2 2_1
Cell dimensions				
a, b, c (Å)	37.31, 94.37, 53.64	38.65, 65.75, 68.65	37.03, 94.79, 53.50	37.11, 95.09, 53.73
α, β, γ (°)	90, 90, 90	90, 90, 90	90, 90, 90	90, 90, 90
Resolution (Å)	1.65-35.43 (1.65-1.68)	2.40-47.49 (2.40-2.49)	1.60-47.40 (1.60-1.62)	1.90-50.00 (1.90-1.93)
Rsym or Rmerge	0.044 (1.635)	0.193 (1.500)	0.029 (0.572)	0.042 (0.273)
I/σI	16.8 (1.2)	9.7 (1.5)	26.9 (2.2)	48.5 (5.1)
$CC_{1/2}$	0.999 (0.636)	0.996 (0.665)	0.999 (0.931)	0.986 (0.892)
Completeness (%)	99.5 (97.9)	99.7 (97.2)	99.2 (86.5)	97.2 (88.9)
Redundancy	4.6 (4.5)	8.7 (8.7)	6.4 (5.8)	8.5 (4.0)
Wavelength (Å)	0.97631	0.975	0.975	1.5406
No. unique reflections	11722	7305	12814	7559
Refinement				
Resolution (Å)	1.65-35.43	2.40-47.49	1.60-35.48	1.90-47.54
Rwork/Rfree	19.04/21.51	22.10/26.18	20.61/25.68	20.51/23.90
No. atoms				
Protein	A- 658, D-57	A-728, B-815	639	622
Ligand/ion	14	4	10	14
Water	41	23	52	53
B-factors				

Protein	A- 39.861, D-76.573	A-44.222, B-47.739	34.768	25.620
Ligand/ion	SO_4-43.610, BCT-57.580	βME-79.395	SO_4-31.602	SO_4-32.880, βME-52.630
Water	43.445	34.486	40.492	30.642
RMSD				
Bond lengths (Å)	0.014	0.006	0.006	0.013
Bond angles (°)	1.602	1.09	0.805	1.598
Ramachandran statistics [a]	P: 75 (98.68%), A: 1 (1.32%), O: 0 (0%)	P: 187 (98.42%), A: 3 (1.58%), O: 0 (0%)	P: 76 (98.70%), A: 1 (1.30%), O: 0 (0%)	P: 77 (98.72%), A: 1 (1.28%), O: 0 (0%)
Missing residues	A- 211, 293-318, D- 211-306, 314-318	A: 307-318. B: 211, 316-318	293-318	211, 293-318

[a] P- Preferred region, A- Allowed region, and O- outliers.

Values in parentheses are for the highest resolution shell.

One crystal was used per dataset.

Data was collected at 100K.

Table 3: Crystallographic software used for solving the structure of MamM CTD mutants.

Protein name	**MamM CTD C267S**	**MamM CTD W247A**	**MamM CTD H264A-E289A-C267S**	**MamM CTD H264A-E289A**
PDB ID	**6G55**	**6G6I**	**6G5E**	**6G64**
Data reduction	XDS [44]	XDS	XDS	HKL2000 [45]
Data scaling	Aimless [46]	Aimless	Aimless	HKL2000
Structure solution method	Molecular replacement – using MamM CTD WT structure (PDB ID: 3W5X)			
Phasing	Phaser MR [47]			
Refinement	Refmac5 [48], PDB-REDO [49]	Phenix [50], PDB-REDO	Refmac5, Phenix	Refmac5, PDB-REDO

Manual refinement was performed using Coot version 0.8.9 [51].

Aimless, Phaser MR and Refmac5 were used through the CCP4i package [52].

Table 4: RMSDs between crystal structures of the different MamM CTD constructs.

Protein name	WT – 3W5X	WT – 3W5Y	PS – 3W66	PS – 3W8P	CS – 6G64
WT – 3W5X	-	0.82	0.88	1.04	0.19
WT – 3W5Y	-	-	1.00	0.74	0.92
PS – 3W66	-	-	-	0.97	0.90
PS – 3W8P	-	-	-	-	1.11
CS – 6G64	-	-	-	-	-

RMSDs between structures (carbon alpha) were calculated using the iterative magic fit tool in SwissPdbViewer [36].

Table 5: Thermodynamic parameters of Zn^{2+} binding to WT and PS determined by ITC.

Parameter	WT [a]	PS [b]
K_D (μM)	31.5 ± 3.4	17.9 ± 2.6
N	2.80 ± 0.24 (3-4) [c]	2.41 ± 0.24 (2) [c]
ΔH (kJ mol^{-1})	-4.20 ± 0.10	-5.42 ± 2.36
K_{ass} (mM^{-1})	32.07 ± 3.22	56.78 ± 7.45
-TΔS (kJ mol^{-1})	-21.51 ± 0.29	-21.69 ± 2.34
ΔG (kJ mol^{-1})	-25.71 ± 0.26	-27.11 ± 0.34
ΔS (J mol^{-1} K^{-1})	72.15 ± 0.98	72.76 ± 7.84

[a] $[WT]_i$ = 50 μM, $[WT]_f$ = 37.45 μM, $[Zn^{2+}]_i$ = 1.4 mM & $[Zn^{2+}]_f$ = 351 μM, ratio: 1:9.4

[b] $[PS]_i$ = 50 μM, $[PS]_f$ = 37.45 μM, $[Zn^{2+}]_i$ = 1.0 mM & $[Zn^{2+}]_f$ = 251 μM, ratio: 1:6.7

[c] N values from PELDOR titrations.

Data were fitted to independent + blank (constant) models in the TA NanoAnalyze Data Analysis software.

Each parameter represents three independent measurements after control reduction (Zn^{2+} at the same concentration, titrated into buffer solution). Errors are reported as the standard deviation.

In all measurements, the sample in cell was in 10 mM Tris-HCl pH 8.0 and 150 mM NaCl, while the titrant Zn^{2+} was in 1 mM Tris-HCl pH=8.0 and 150 mM NaCl.

Table 6: Kinetic parameters for Zn^{2+} binding to MamM CTD WT and PS.

Parameter	WT	PS
k_{+ps}^{CC} // k_{+csm}^{s} (sec^{-1})	39.2 ± 1.4	29.4 ± 1.6
K_{PS} ($1/K_{PS}$) (μM)	62.6 ± 13.0	19.4 ± 17.2
$K_{PS}\ k_{+ps}^{CC}$ (μM sec^{-1}) [a]	0.63 ± 0.14	-
k_{-ps}^{CC} // $k_{-csm}^{s} + k_{+csm}^{s}$ (sec^{-1})	0.52 ± 2.32	95.1 ± 40.4
k_{-csm}^{s} (sec^{-1})	-	65.7 ± 38.8
K_{CSM}^{S}	-	0.45 ± 0.27
$k_{diss,fast}$ (sec^{-1})	2.4 ± 0.1	4.6 ± 0.1
$k_{diss,slow}$ (sec^{-1})	0.20 ± 0.07	0.46 ± 0.02
K_H (μM) [b]	33.9 ± 1.3	39.5 ± 2.2
n_H [b]	1.61 ± 0.13	2.1 ± 0.2

[a] Relates to WT.

[b] Determined from the total amplitudes.

Left parameters relate to WT, right parameters relate to PS.

Conditions were as follows: 10 mM Tris (pH 8.0) and 150 mM NaCl at 25 °C.

Schema

Scheme 1:

$$\left[\mathrm{CTD^{O}} + \mathrm{Zn^{2+}} \underset{(\textit{dead time})}{\overset{K_{CS}}{\rightleftharpoons}} \mathrm{CTD^{C}(Zn^{2+})}\right] + 2\cdot\mathrm{Zn^{2+}} \underbrace{\overset{\frac{K_{PS}}{k_{+ps}}}{\underset{k_{-ps}}{\rightleftharpoons}}}_{(\textit{rapid EQ})} \mathrm{CTD^{C}Zn^{2+}\cdot(Zn^{2+})_2} \underbrace{\overset{\frac{K_{PS}^{CC}}{k_{+ps}^{CC}}}{\underset{k_{-ps}^{CC}}{\rightleftharpoons}}}_{(\textit{slow})} \mathrm{CTD^{CC}(Zn^{2+})_3}$$

Scheme 2:

$$\mathrm{CTD^{SO}_{CSM}} \underbrace{\overset{\frac{K_{CSM}^{S}}{k_{+csm}^{s}}}{\underset{k_{-csm}^{s}}{\rightleftharpoons}}}_{(\textit{slow})} \mathrm{CTD^{SC}_{CSM}} + \mathrm{(Zn^{2+})_2} \underbrace{\overset{\frac{K_{CSM}^{PS}}{k_{+csm}^{ps}}}{\underset{k_{-csm}^{ps}}{\rightleftharpoons}}}_{(\textit{rapid})} \mathrm{CTD^{SCC}_{CSM}\cdot(Zn^{2+})_2}$$

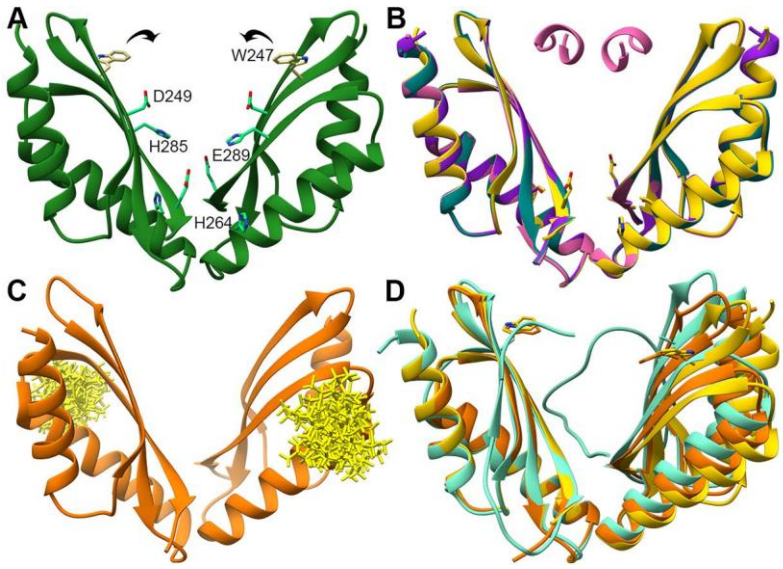

Figure 1: MamM CTD crystal structures and models. (A) The dimeric apo MamM CTD WT structure (PDB ID: **3W5X**). The binding site residues (D249, H264, H285, E289, light green) and the fluorescence-active tryptophan residue (W247, yellow) are indicated. Black arrows correspond to the proposed movement of the monomers toward each other. (B) The new crystal structures of C267S (pink, PDB ID: **6G55**), CS-C267S (purple, PDB ID: **6G5E**) and CS (cyan, PDB ID: **6G64**) overlapped onto the WT structure (yellow, PDB ID: **3W5X** [13]). All mutation site residues (both in mutants and WT proteins) are indicated as sticks. (C) Using the PDB ID: **3W5Y** [13] an MMM-modelled structure of WT MamM CTD is presented including the computed rotamer library of MTSL spin labels attached to position C275 [22]. (D) The new crystal structure of W247A (light blue, PDB ID: **6G6I**) overlapped onto the WT structures (PDB ID: **3W5X** in yellow and PDB ID: **3W5Y** in orange). All mutation site residues (both in mutants and WT proteins) are indicated as sticks.

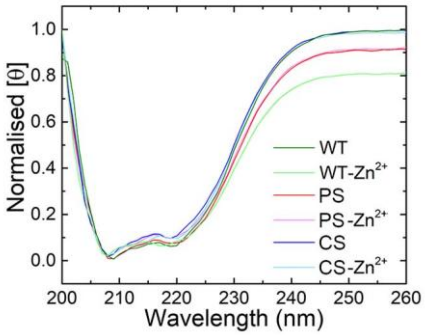

Figure 2: CD spectra of MamM CTD in the apo and metal-bound forms. To ensure that no metals are bound to MamM CTD proteins, proteins were pre-incubated with EDTA for 5 hours, which was subsequently removed by dialysis over-night. The proteins were diluted to a final concentration of 0.3 mg mL^{-1}, with or without Zn^{2+} (15:1 Zn^{2+} to protein ratio), and spectral profiles were measured in a wavelength range of 200-260 nm. Darker colors refer to the apo forms and lighter colors to the metal-bound forms; WT in green, PS in red and CS in blue.

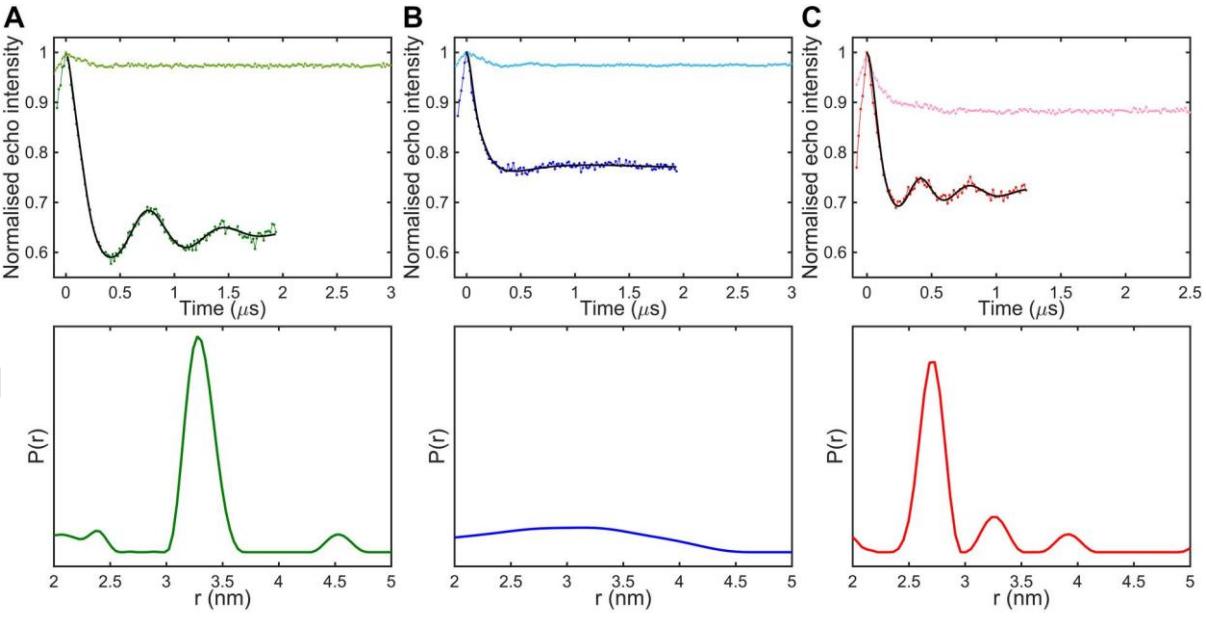

Figure 3: Four-pulse PELDOR experiments of doubly spin-labelled MamM CTD constructs containing C275, in both apo and Zn^{2+}-bound forms, measured at 60 K. (Top panel) Green, blue and red traces are the normalized background-corrected dipolar evolution of (A) C267S, (B) CS-C267S and (C) PS-C267S MamM CTD respectively. The traces for both apo and Zn^{2+}-bound forms are presented in light and dark colors, respectively. All raw time traces were subjected to a first-order

polynomial background correction. Fittings of Zn^{2+}-bound corrected traces are shown as black lines. (Bottom panel) Distance distributions of Zn^{2+}-bound MamM CTD constructs (A) C267S, (B) CS-C267S and (C) PS-C267S. Fitting of all the dipolar evolutions and subsequent distance distributions were calculated with DeerAnalysis2016 [23] using a Tikhonov regularisation.

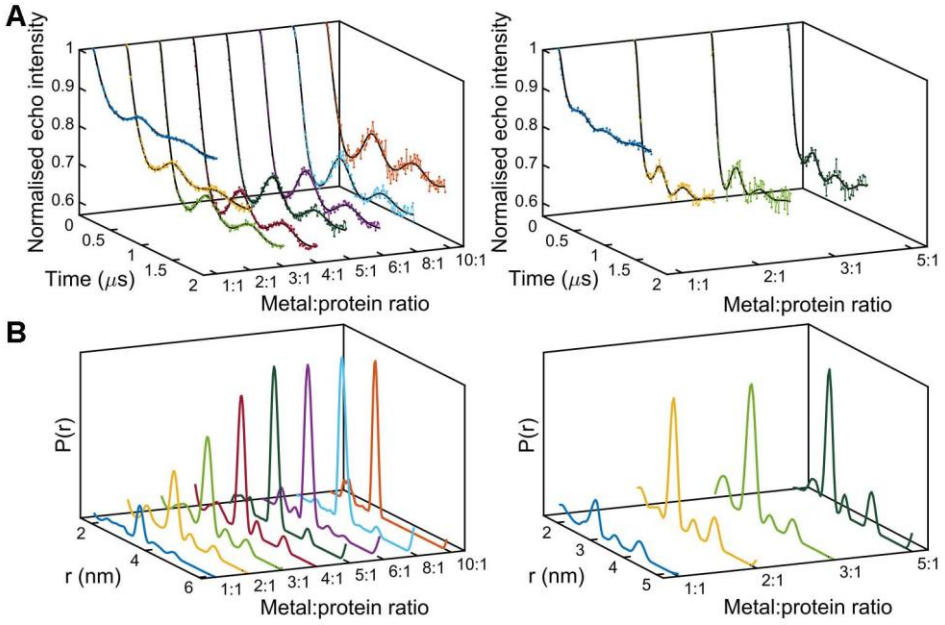

Figure 4: Four-pulse PELDOR titrations of doubly spin-labelled MamM CTD C267S and PS-C267S constructs containing C275, measured at 60 K. (A) The normalised and background-corrected dipolar evolution of C267S (left) and PS-C267S (right) MamM CTD following Zn^{2+} titration, with metal:protein ratios ranging from 1:1 to 10:1 excess and 1:1 to 5:1 excess, respectively (coloured lines). All raw time traces were subjected to a first-order polynomial background correction. Spectral fittings are shown as black lines. (B) Distance distributions corresponding to each titre of Zn^{2+}-bound C267S (left) and PS-C267S (right). Fitting of the dipolar evolutions and subsequent distance distributions were calculated with DeerAnalysis2016 [23] using a Tikhonov regularisation.

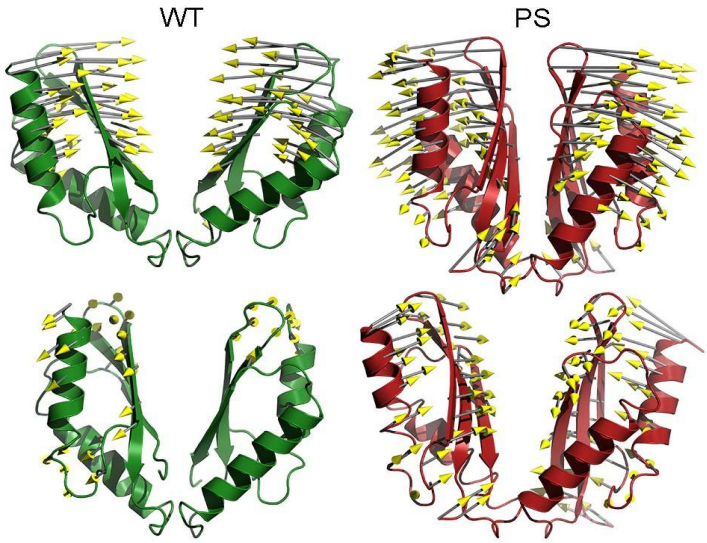

Figure 5: Complex dynamics as described by the two set frequencies mode 7 (the native-like open-close movement, top panel) and mode 8 (the swiveling movement, bottom panel) of WT (green, left) and PS (red, right). Size and direction of motions along the modes are represented by arrows.

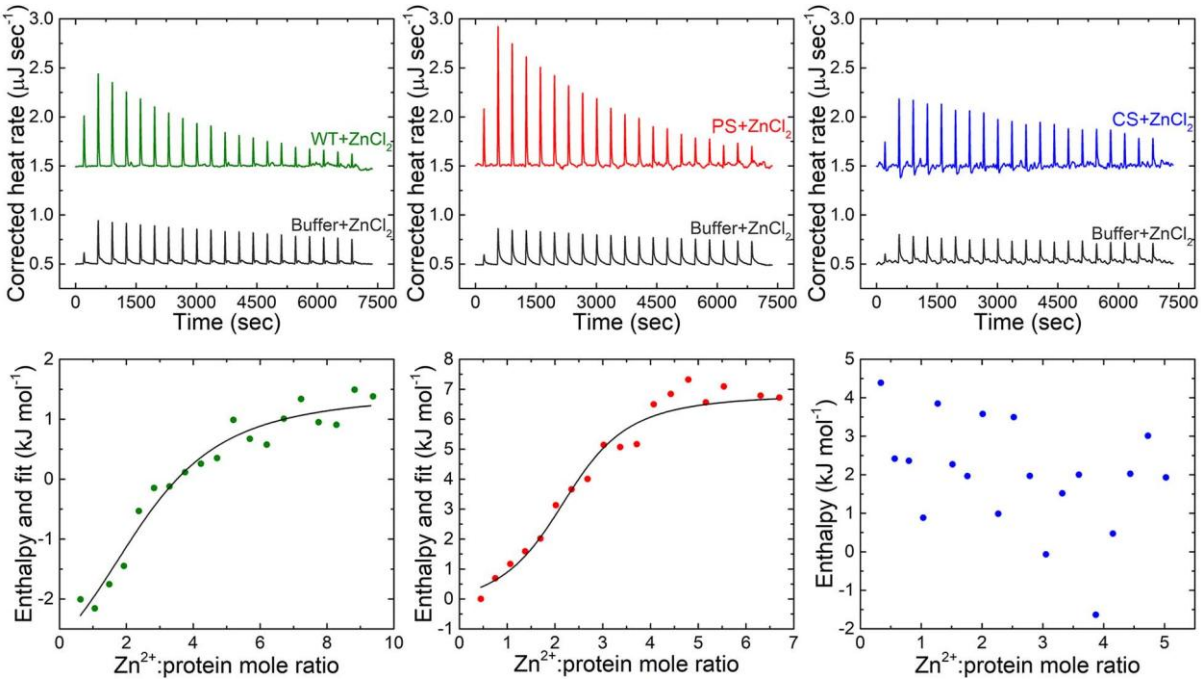

Figure 6: ITC measurements of MamM CTD-Zn^{2+} interactions. (Top panel) Corrected heat rate time curves for a representative titration for each MamM CTD construct with Zn^{2+}. For each protein (left- WT in green, middle- PS in red and right- CS in blue), the heat flow curve of the control (Zn^{2+}

titration in buffer, gray) is given as a reference. (Bottom panel) Titration data after peak integration as a function of molar ratio, and data fitting for both WT and PS. See Table 5 for binding parameters of WT and PS.

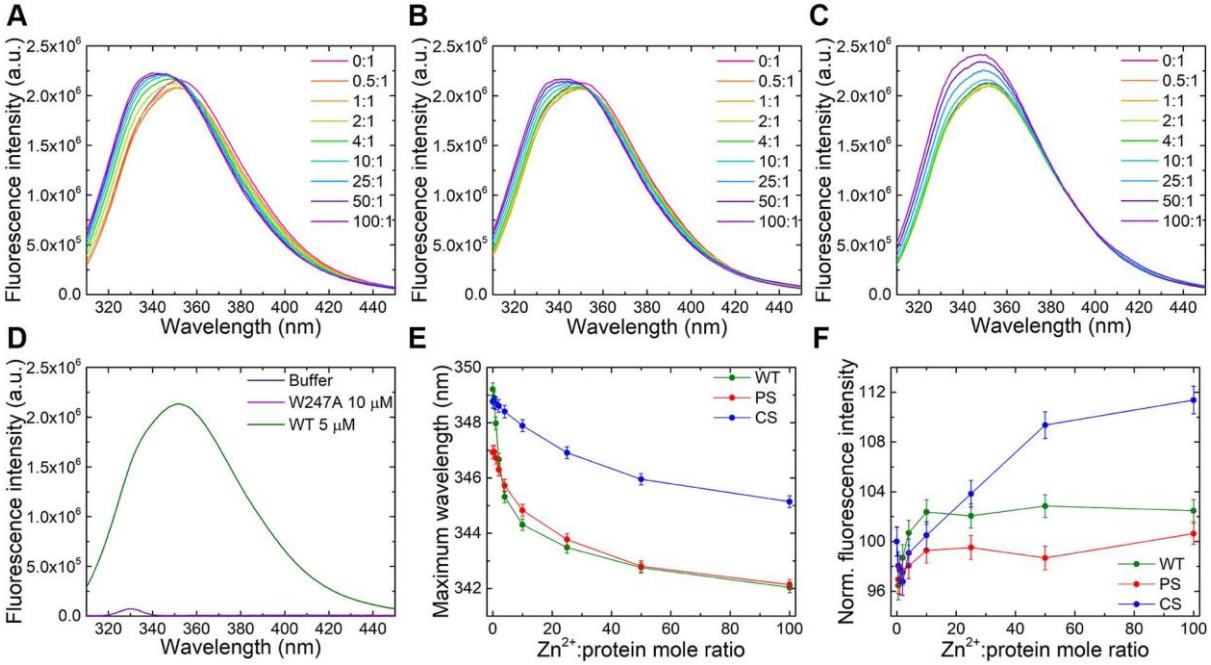

Figure 7: Fluorescence scans of MamM CTD constructs with varying Zn^{2+} concentrations. MamM CTD proteins at 5 μM concentration were titrated using a $ZnCl_2$ solution to reach different MamM CTD:Zn^{2+} ratios (intensity was normalized due to the change in MamM CTD concentration) and emission spectra were recorded. Samples were measured at an excitation of λ_{ex} 297 nm and the emission spectrum for each $ZnCl_2$ concentration was recorded between 310-450 nm. For each protein, the data presented is the average of three independent measurements. (A) Emission spectra of WT with different Zn^{2+} concentrations, (B) Emission spectra of PS with different Zn^{2+} concentrations, (C) Emission spectra of CS with different Zn^{2+} concentrations, (D) Emission spectra of 5 μM WT, 10 μM D247A and buffer as a control, (E) λ_{max} as function of MamM CTD:Zn^{2+} ratio (WT in green, PS red and CS in blue), (F) Normalized fluorescence intensity compared to no Zn^{2+} as function of MamM CTD:Zn^{2+} ratio (WT in green, PS red and CS in blue). Errors are reported as the standard deviation.

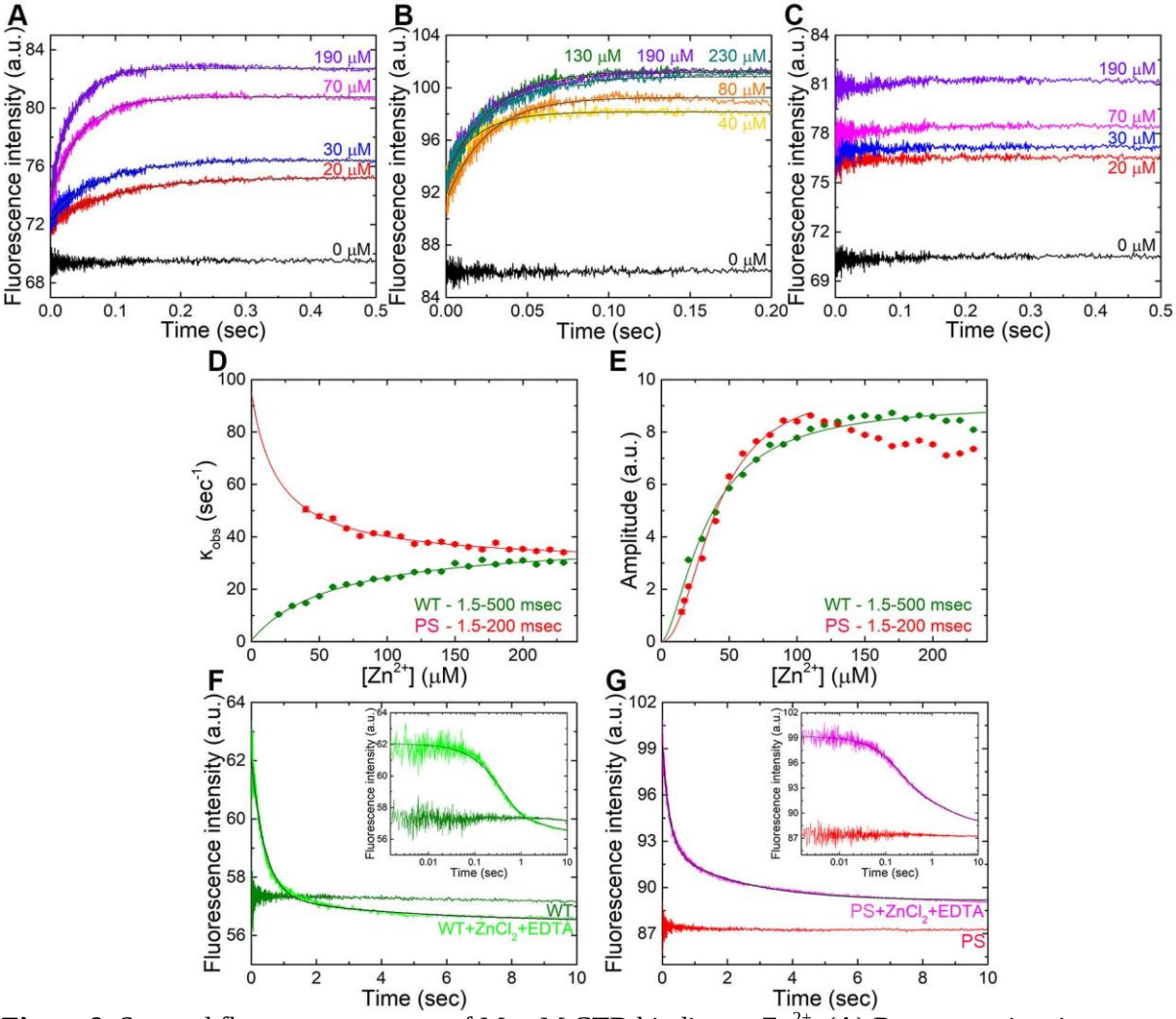

Figure 8: Stopped flow measurements of MamM CTD binding to Zn^{2+}. (A) Representative time courses of WT tryptophan fluorescence enhancement after a rapid mixing of WT (2.5 µM, final protein concentration) with different Zn^{2+} concentrations. Datasets are averaged transients (n=2 and for each n, at least 3 repeats were also averaged). Datasets were fitted to Equation 4 using n=1. (B) Representative time courses of PS tryptophan fluorescence enhancement after a rapid mixing of WT (2.5 uM, final concentration) with different Zn^{2+} concentrations. Datasets are averaged transients (n=2 and for each n, at least 3 repeats were averaged). Datasets were fitted to Equation 4 using n=1. (C) Representative time courses of CS tryptophan fluorescence enhancement after a rapid mixing of CS (2.5 µM, final concentration) with different Zn^{2+} concentrations. Datasets are averaged transients (using n=2 while for each n, at least 3 repeats were averaged). (D) k_{obs} of WT (green) and PS (red) plotted as function of Zn^{2+} concentration. Datasets were fitted to a hyperbolic function (Equations 1 & 3). For PS, only the 2nd phase (40-230 µM Zn^{2+}) could be fitted. Error bars are shown within the symbols. (E) Amplitude of WT and PS plotted as function of Zn^{2+} concentration. Datasets were fitted to the Hill equation (Equation 2) for WT and PS's first phase (15-110 µM Zn^{2+}). Error bars are shown within the symbols. (F)+(G) Zn^{2+} dissociation experiments for MamM CTD: Representative time

courses of tryptophan fluorescence enhancement after a rapid mixing of: (F) dark green – 2.5 µM WT with buffer, light green – 2.5 µM WT + 150 µM Zn^{2+} with 2.5 mM EDTA, (G) red – 2.5 µM PS with buffer, magenta – 2.5 µM PS + 150 µM Zn^{2+} with 2.5 mM EDTA (final concentrations). Datasets are averaged transients (with n=1, at least 4 repeats were averaged). Datasets were fitted using Equation 4 with n=2. Insets: the same data presented on a logarithmic scale.

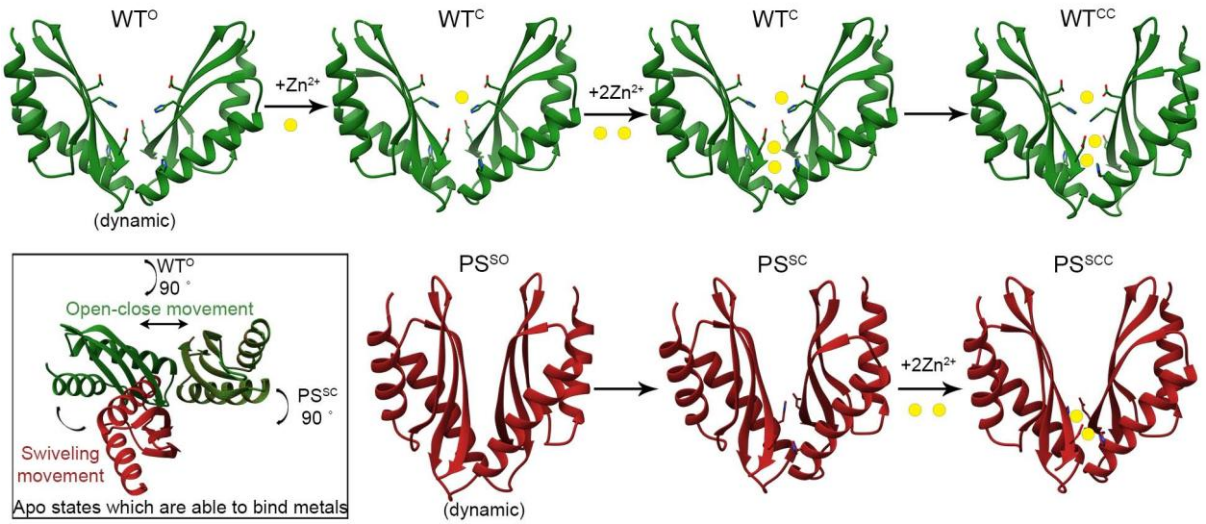

Figure 9: A binding mechanism model for WT and PS. Top row, green- A three step binding mechanism for WT as described in Scheme 1: first a rapid step in which one Zn^{2+} binds to the central site, followed by fast Zn^{2+} binding to the peripheral sites and a slower isomerization step to achieve the final, three-ion bound closed state. Bottom row, red- A two-step binding mechanism for PS as described in Scheme 2: a slow step in which an isomerization between different apo swiveling forms occurs, followed by fast Zn^{2+} binding to the peripheral sites that is only allowed by one apo form, and packing of the dimer to a similar, but yet tighter conformation than that of the WT. Lower left box; An overlapped representation of the WT^{O} and PS^{SC} forms to demonstrate the difference between the swiveling movement and the standard CTD's closure movement.

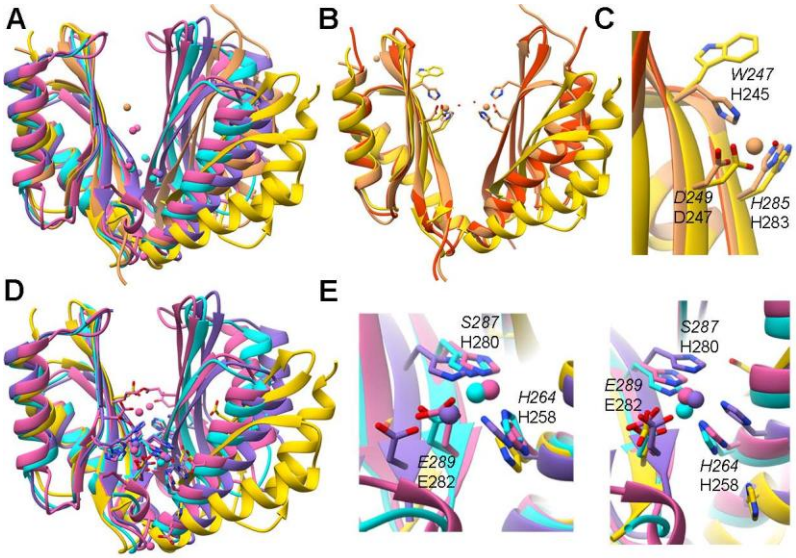

***Figure 10*:** CDF protein CTDs conserved binding sites. (A) The dimeric CTD crystal structures of Zn^{2+}-bound MamB (light orange, PDB ID: **5HO1**[14]), Zn^{2+}-bound CzrB (pink, PDB ID: **3BYR**[12]), Zn^{2+}-bound *E. coli* YiiP (blue, PDB ID: **3H90**[9]) and Zn^{2+}-bound *S. oneidensis* YiiP (purple, PDB ID: **5VRF**[10]) overlapped onto the dimeric apo MamM CTD WT structure (yellow, PDB ID: **3W5X**[13]). For all the bound structures, the Zn^{2+} ions are indicated in the structure color. (B) The dimeric crystal structures of Zn^{2+}-bound MamB CTD (light orange) and apo MamB CTD (dark orange, PDB ID: **5HO5**[14]) overlapped onto the dimeric apo MamM CTD WT structure (yellow). MamB's Zn^{2+} ions, the Zn^{2+} ions chelating water molecules, MamB's central binding site residues and their homologous residues from MamM are indicated as sticks. (C) Magnification of the monomeric central binding site of MamB and MamM. The residues are labeled so that the upper labels in *italics* refer to MamM's residues and the lower labels to MamB's residues. The D249 and H285 residues in MamM CTD central binding site are conserved in MamB, where they were shown to participate directly in the chelation of the metal ion. (D) The dimeric CTD crystal structures of Zn^{2+}-bound CzrB (pink), Zn^{2+}-bound *E. coli* YiiP (blue) and Zn^{2+}-bound *S. oneidensis* YiiP (purple) overlapped onto the dimeric apo MamM CTD WT structure (yellow). All proteins' bound Zn^{2+} ions, all the Zn^{2+} ions binding site residues and their homologous residues from MamM are indicated as sticks. (E) Magnifications of the peripheral binding site of CzrB, YiiP proteins and MamM (only this site is shown for clarity). The residues are labeled so that the upper labels in *italics* refer to MamM's residues and the lower labels to CzrB's residues. The H264 (left panel) and E289 (right panel) residues in MamM CTD peripheral binding site are conserved in YiiP and CzrB proteins, where they were shown to participate directly in the chelation of the Zn^{2+} ion.

Supporting Information

Appendix S1: Derivation of Equation 3 for the PS kinetic model.